

Long-lived topological time-crystalline order on a quantum processor

Liang Xiang,^{1,*} Wenjie Jiang,^{2,*} Zehang Bao,^{1,*} Zixuan Song,¹ Shibo Xu,¹ Ke Wang,¹ Jiachen Chen,¹ Feitong Jin,¹ Xuhao Zhu,¹ Zitian Zhu,¹ Fanhao Shen,¹ Ning Wang,¹ Chuanyu Zhang,¹ Yaozu Wu,¹ Yiren Zou,¹ Jiarun Zhong,¹ Zhengyi Cui,¹ Aosai Zhang,¹ Ziqi Tan,¹ Tingting Li,¹ Yu Gao,¹ Jinfeng Deng,¹ Xu Zhang,¹ Hang Dong,¹ Pengfei Zhang,¹ Si Jiang,² Weikang Li,² Zhide Lu,² Zheng-Zhi Sun,² Hekang Li,¹ Zhen Wang,^{1,3} Chao Song,¹ Qiujiang Guo,^{1,3,†} Fangli Liu,^{4,5} Zhe-Xuan Gong,^{6,7} Alexey V. Gorshkov,⁴ Norman Y. Yao,⁸ Thomas Iadecola,^{9,10} Francisco Machado,^{8,11} H. Wang,^{1,3,‡} and Dong-Ling Deng^{2,3,12,§}

¹*School of Physics, ZJU-Hangzhou Global Scientific and Technological Innovation Center, and Zhejiang Province Key Laboratory of Quantum Technology and Device, Zhejiang University, Hangzhou, China*

²*Center for Quantum Information, IIIS, Tsinghua University, Beijing 100084, China*

³*Hefei National Laboratory, Hefei 230088, China*

⁴*Joint Quantum Institute and Joint Center for Quantum Information and Computer Science, NIST and University of Maryland, College Park, MD, USA*

⁵*QuEra Computing Inc., Boston, MA, USA*

⁶*Department of Physics, Colorado School of Mines, Golden, CO, USA*

⁷*National Institute of standards and Technology, Boulder, CO, USA*

⁸*Department of Physics, Harvard University, Cambridge 02138 MA, USA*

⁹*Department of Physics and Astronomy, Iowa State University, Ames, IA, USA*

¹⁰*Ames Laboratory, Ames, IA, USA*

¹¹*ITAMP, Harvard-Smithsonian Center for Astrophysics, Cambridge, Massachusetts, 02138, USA*

¹²*Shanghai Qi Zhi Institute, 41th Floor, AI Tower, No. 701 Yunjin Road, Xuhui District, Shanghai 200232, China*

Topologically ordered phases of matter [1–3] elude Landau’s symmetry-breaking theory [4], featuring a variety of intriguing properties such as long-range entanglement and intrinsic robustness against local perturbations. Their extension to periodically driven systems gives rise to exotic new phenomena that are forbidden in thermal equilibrium [5, 6]. Here, we report the observation of signatures of such a phenomenon—a prethermal topologically ordered time crystal—with programmable superconducting qubits arranged on a square lattice. By periodically driving the superconducting qubits with a surface-code Hamiltonian [7, 8], we observe discrete time-translation symmetry breaking dynamics [9–16] that is only manifested in the subharmonic temporal response of nonlocal logical operators. We further connect the observed dynamics to the underlying topological order by measuring a nonzero topological entanglement entropy [17, 18] and studying its subsequent dynamics. Our results demonstrate the potential to explore exotic topologically ordered nonequilibrium phases of matter with noisy intermediate-scale quantum processors [19].

Phases of matter are often classified by broken symmetries and local order parameters [4]. However, the discovery of topological order has transformed this simple paradigm [1, 2]. Two topologically ordered phases with the same symmetries can showcase topologically distinct features, such as different patterns of long-range entanglement and the emergence of quasiparticles with different anyonic braiding statistics [3, 20, 21]. These features are intrinsically nonlocal in that they cannot be distinguished by any local order parameter [7, 22]. Unfortunately, topological order is usually restricted to the ground state; mobile thermal excitations can hybridize nominally degenerate ground states by traversing the system along nontrivial closed loops. By introducing disorder, the motion of these excitations can be arrested and the hybridization process suppressed. In the limit where excitations are fully localized, the topological phase becomes stable across the entire energy spectrum of the system [5, 6, 23–29].

Time-periodic driving of a quantum many-body system enables novel phases of matter that cannot exist in thermal equilibrium. A prominent example is that of time crystals [9–16], where discrete time translation symmetry is spontaneously broken. Strikingly, the concept of a time crystal can be ex-

tended to include topological order, resulting in a new dynamical phase dubbed a topologically ordered time crystal [30]. Unlike conventional time crystals, where the breaking of time translation symmetry manifests in the dynamics of local observables, topologically ordered time crystals show such symmetry breaking only for nonlocal logical operators. Whether or not this phase has a truly infinite lifetime depends on the late-time stability of many-body localization [31–33]; nevertheless, the dynamical features of the system can still exhibit very long-lived signatures of localization persisting beyond current experimental timescales. While signatures of conventional time crystals without topological order have been observed in a number of distinct systems, including trapped ions [34, 35], spins in nitrogen-vacancy centers [36, 37], ultracold atoms [38, 39], solid-state spin ensembles [40–42], and superconducting qubits [13, 43, 44], the observation of a topologically ordered time crystal remains an open challenge.

Here, we report the observation of a long-lived prethermal topologically ordered discrete time crystal, with eighteen programmable superconducting transmon qubits arranged on a two-dimensional square lattice. By optimizing the device fabrication and control process, we push the median lifetime of

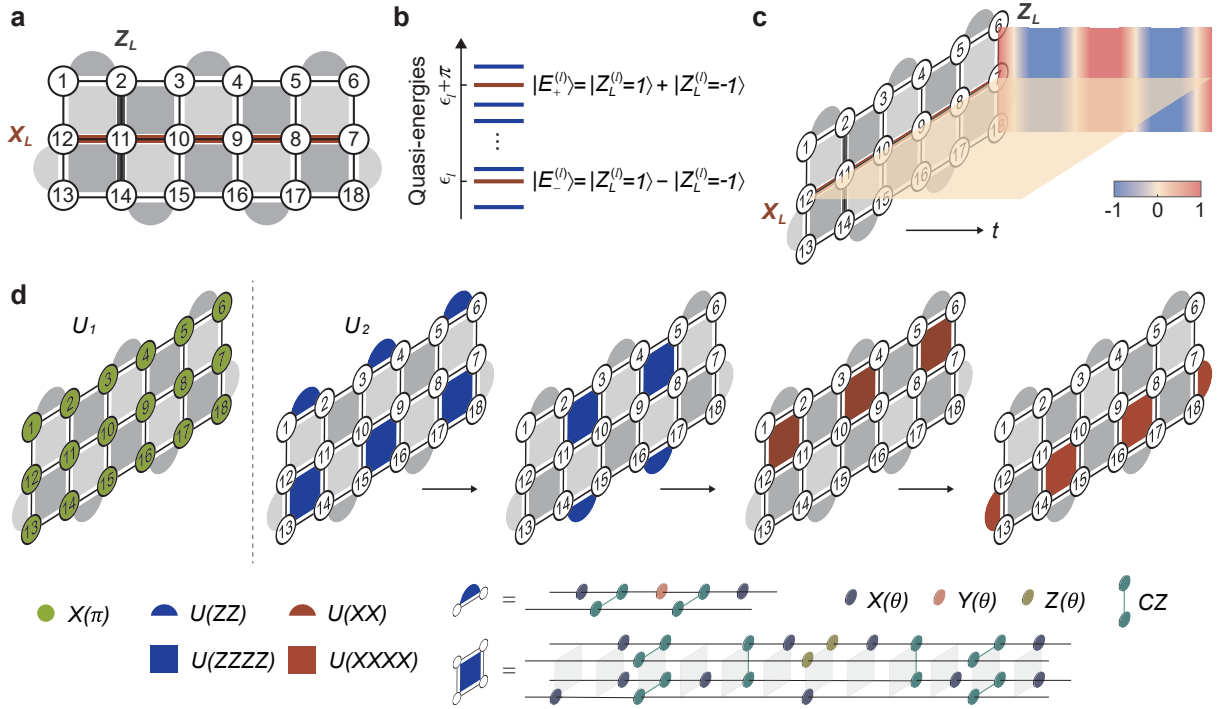


FIG. 1. **Periodically driven surface code model.** **a**, Rotated surface code model on a three-by-six square lattice. The circled numbers label the qubits. The dark and light gray regions represent plaquette operators A_p and B_q , respectively. The thick black (red) line represents the nonlocal string operator Z_L (X_L). **b**, Topologically ordered Floquet eigenstates in the limit $B \rightarrow 0$. The quasi-energies of each pair of eigenstates $|E_{\pm}^{(l)}\rangle$ are split by π . **c**, Schematic of the stroboscopic dynamics of the string operators Z_L and X_L . Under periodic driving, the expectation value of Z_L exhibits a persistent subharmonic oscillation with a period of $2T$, while X_L preserves a constant value of zero. **d**, Decomposition of the Floquet unitary U_F ($B = 0$) into elementary quantum gates. U_1 is realized by applying π pulses to all the qubits. Since all the plaquette operators commute with each other, U_2 is constructed by sequentially applying four groups of them. Plaquette unitaries $e^{-iA_p T/2}$, labeled by $U(ZZZZ)$ and $U(ZZ)$, and $e^{-iB_q T/2}$, labeled by $U(XXXX)$ and $U(XX)$, are further decomposed into sequences of single-qubit rotations and two-qubit controlled-Z gates. $X(\theta)$, $Y(\theta)$, and $Z(\theta)$ denote single-qubit rotations by an angle θ around the x -, y -, and z -axis, respectively. $e^{-iB_q T/2}$ can be implemented by sandwiching $e^{-iA_q T/2}$ with Hadamard gates. In the experiment, the whole circuit is further compiled to reduce the depth and suppress hardware noise (Supplementary Section II.E).

these qubits to $T_1 \approx 163 \mu\text{s}$ and the median simultaneous single- and two-qubit gate fidelities above 99.9% and 99.4%, respectively. Together with a neuroevolution algorithm [45] that outputs near-optimal quantum circuits for digitally simulating four-body interactions, this enables us to successfully implement Floquet surface-code dynamics with an optimized quantum circuit of depth exceeding 700, consisting of more than 2300 single- and 1400 two-qubit gates. We measure the dynamics of nonlocal logical operators and local spin magnetizations and find that the former show a robust subharmonic response, whereas the latter decay quickly to zero and do not show period-doubled oscillations. This differs drastically from conventional discrete time crystals, where local, rather than nonlocal, observables exhibit subharmonic response. We further reveal the long-range quantum entangled nature of topological order by preparing a many-body eigenstate of the Floquet unitary and measuring its topological entanglement entropy with different subsystem sizes and geometries [17, 18]. We obtain near-expected values for the measured topological entanglement entropy, which deviates significantly from the trivial-state value of zero and provides

strong evidence for the presence of topological order.

Theoretical model and experimental setup

We consider the periodically driven rotated surface code model on a 2D lattice with open boundary conditions [30, 46]:

$$\begin{aligned}
 H(t) &= \begin{cases} H_1, & 0 \leq t < T', \\ H_2, & T' \leq t < T, \end{cases} \\
 H_1 &\equiv \frac{\pi}{2} \sum_k \sigma_k^x + \sum_k \mathbf{B}_k \cdot \boldsymbol{\sigma}_k, \\
 H_2 &\equiv - \sum_p \alpha_p A_p - \sum_q \beta_q B_q,
 \end{aligned} \tag{1}$$

where $\boldsymbol{\sigma}_k = (\sigma_k^x, \sigma_k^y, \sigma_k^z)$ is a vector of Pauli matrices acting on the k -th qubit; \mathbf{B}_k denotes an on-site field drawn randomly and independently from a ball with radius B ; the plaquette operators $A_p = \prod_{m \in p} \sigma_m^z$ and $B_q = \prod_{n \in q} \sigma_n^x$ are products of Pauli operators on the corresponding plaquettes (Fig. 1a);

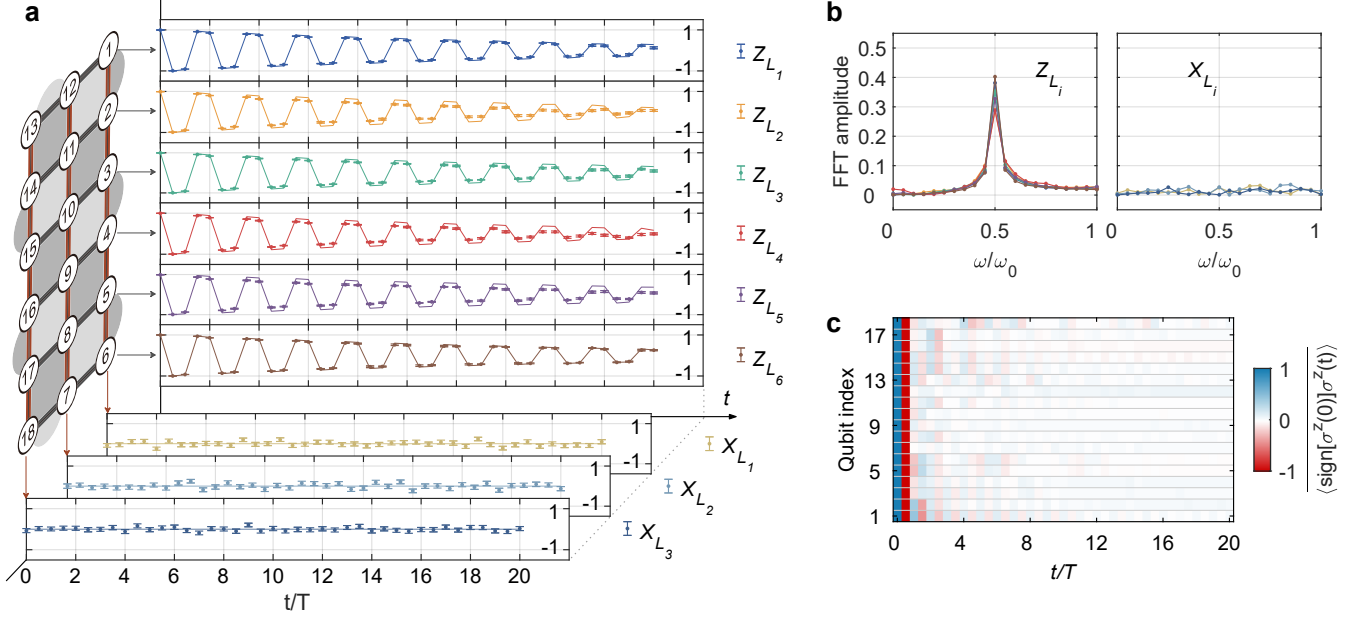


FIG. 2. Time-translation symmetry breaking for nonlocal observables with $B = 0$. **a**, Dynamics of nonlocal observables. Auto-correlation function for the three-body string operators $\{Z_{L_i}\}$ (thick black lines) and the six-body string operators $\{X_{L_i}\}$ (thick red lines) are shown in the upper six and lower three panels, respectively. Experimental data points (dots) are obtained from averaging over 24 random realizations, with error bars representing the standard error of the statistical mean. The numerical results (lines) are computed by taking into account qubit decoherence and gate errors (Supplementary Section III). Whereas the expectation values for $\{X_{L_i}\}$ remain zero, the auto-correlators for $\{Z_{L_i}\}$ exhibit stable subharmonic oscillations for up to 20 cycles. **b**, Fourier spectra of time-domain signals observed in **a**, where a stable subharmonic frequency peak appears for $\{Z_{L_i}\}$ but not $\{X_{L_i}\}$. **c**, Dynamics of the auto-correlation function for local observables $\{\sigma_k^z\}$. Such auto-correlations decay quickly to zero, in sharp contrast to those of the string operators $\{Z_{L_i}\}$.

α_p and β_q are coefficients uniformly chosen from $[0, 2\pi)$; the drive period is fixed as $T = 2T' = 2$, which roughly corresponds to a $1.4\text{-}\mu\text{s}$ runtime for the corresponding quantum circuit in our experiment.

We note that, other than the discrete time-translation symmetry, $H(t)$ breaks all microscopic symmetries due to the presence of the random on-site fields B_k in H_1 . The Floquet unitary that fully characterizes the dynamics of the system reads $U_F = U_2 U_1$, with $U_1 = e^{-iH_1}$ and $U_2 = e^{-iH_2}$ being the unitary operators generated by the Hamiltonians H_1 and H_2 , respectively. H_2 represents the Hamiltonian of the rotated surface code model, whose energy spectrum is two-fold degenerate and whose eigenstates show topological order [7, 8]. Owing to their topological nature, the degenerate eigenstates can only be distinguished by nonlocal string operators such as $Z_L = \prod_{k \in P_z} \sigma_k^z$ or $X_L = \prod_{k \in P_x} \sigma_k^x$, which traverse the lattice through the path P_z or P_x (see Fig. 1a). We label each eigenstate pair by $|Z_L^{(l)} = \pm 1\rangle$ for each eigenstate with quasi-energy ϵ_l (see Supplementary Section I.A). In the limit $B \rightarrow 0$, U_1 represents a perfect flip of all spins. As a result, the drive H_1 reorganizes the topologically ordered eigenstate pairs of H_2 into Floquet eigenstates $|E_{\pm}^{(l)}\rangle$ of the form $|E_{\pm}^{(l)}\rangle \propto |Z_L^{(l)} = 1\rangle \pm |Z_L^{(l)} = -1\rangle$. The quasi-energies of the corresponding cat-like eigenstates are split by quasi-energy π (Fig. 1b). As a result, the stroboscopic dynamics of the nonlocal operator Z_L exhibits a stable subharmonic oscillation with

$2T$ periodicity as illustrated in Fig. 1c, which breaks the discrete time-translation symmetry by the drive period T (Supplementary Section I.D). These Floquet eigenstates also exhibit topological order, which is essential for the robustness of the subharmonic response of the nonlocal string operators Z_L .

For small but finite B , the system's integrability is broken and the eigenstate pairs are no longer exactly split by π . However, this deviation arises from the motion of excitations across the system which mixes the different topological sectors, which is strongly suppressed by the disorder in α_p and β_p . Until this thermalization occurs, $t \lesssim t_{\text{th}}$, the system's dynamics will exhibit robust period doubling dynamics, much like in the $B = 0$ case. All our experimental and theoretical observations of period doubling behavior pertain to this “prethermal” regime which, in the small- B regime, is much larger than the experimentally accessible timescales.

Our experiments are carried out on a programmable flip-chip superconducting processor with 18 transmon qubits arranged on a 2D square lattice (see Supplementary Section II.A for detailed information about the device). To implement $H(t)$, the four-body terms with random strengths in H_2 , which are vital for the eigenstate topological order at high energy, pose an apparent challenge since four-body interactions do not naturally appear in the superconducting system. We therefore exploit the idea of digital quantum simulation to

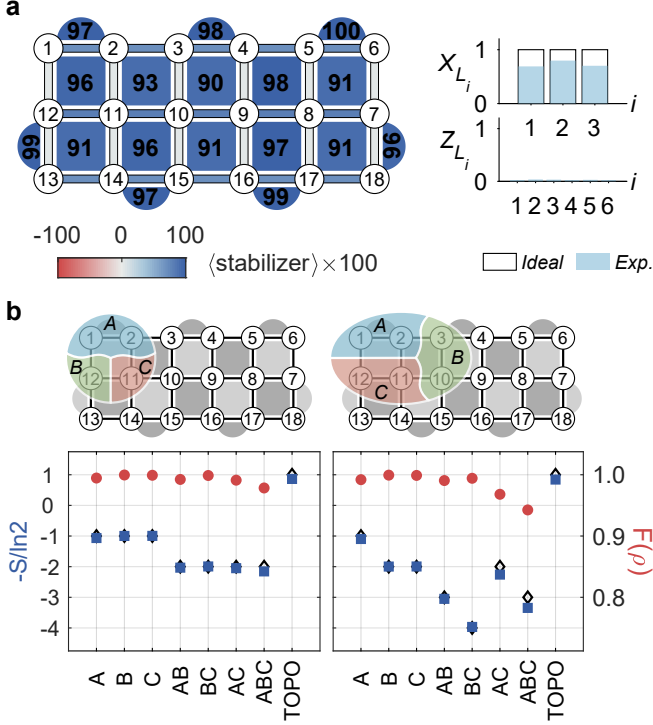


FIG. 3. **Measured stabilizer values and topological entanglement entropy for a Floquet eigenstate.** **a**, Measured expectation values of plaquette operators $\{A_p\}$ and $\{B_q\}$ for the Floquet eigenstate $|E_+^{(0)}\rangle$ are shown in the left panel. Expectation values of string operators $\{X_{L_i}, Z_{L_i}\}$ are plotted in the right panel with solid (hollow) bars representing experimental (theoretical) results. **b**, Measuring topological entanglement entropy (TOPO, S_{topo}) on four- and six-qubit subsystems. Division of subsystems and corresponding experimental results are shown in the upper and lower panels, respectively. Blue squares (red circles) represent entanglement entropy (region fidelities $F(\rho_i)$). The topological entanglement entropy is extracted from the measured von Neumann entropy for the regions S_i . The error bars, obtained by repeated measurements, are very small and not shown here. The black rhombus markers are theoretical predictions for S_{topo} and S_i , which agree well with the corresponding experimental results.

implement $H(t)$ with quantum circuits (Fig. 1d), which are obtained via a neuroevolution algorithm [45] (Supplementary Section I.E). We mention that these quantum circuits are near-optimal and can implement $H(t)$ in an analytical fashion without any Trotter error, independent of α_p , β_p , and B_k . With these efficient quantum circuits, improved gate fidelities, and coherence times, we are able to implement and probe the unconventional dynamics of the system up to 20 driving periods.

Subharmonic response for nonlocal observables

The characteristic signature of topological time-crystalline eigenstate order is the breaking of the discrete time-translation symmetry for nonlocal logical operators, manifested by persistent oscillations with period $2T$. To this end, we define the normalized auto-correlation function $A_L^{1/d}(t) =$

$\text{sign}[\langle Z_L(0)Z_L(t) \rangle] |\langle Z_L(t) \rangle|^{1/d}$ for the d -body string operator Z_L , where $\langle \dots \rangle$ represents the expectation value and the d -th root is used to indicate the geometric mean value. We begin by studying the evolution of the disorder-averaged auto-correlator $A_{L_i}^{1/d}(t)$ for operators $\{Z_{L_i}\}$ ($d=3$) at the solvable limit $B=0$, which are averaged over 24 random realizations by sampling Hamiltonian parameters α_p, β_q and initial product states. From Fig. 2a, it is evident that, in the topologically ordered regime, $A_{L_i}^{1/d}(t)$ oscillates with a $2T$ periodicity for up to 20 driving cycles. We mention that $A_{L_i}^{1/d}(t)$ exhibits a gradually decaying envelope due to extrinsic experimental imperfections, rather than internal thermalization, which is confirmed by numerical simulations (lines in Fig. 2a) incorporating experimentally measured gate errors and decoherence times. Indeed, the ideal numerical simulations show that the internal thermalization time of the system without experimental noise is far longer than 20 driving cycles (Supplementary Section I.C). In the frequency domain, $A_{L_i}^{1/d}$ shows a peak at the subharmonic frequency of the drive period $\omega/\omega_0 = 0.5$, as shown in Fig. 2b. We also note that the string operator X_L does not show period-doubled oscillations, and no subharmonic peak is observed in the frequency domain.

Although the $2T$ -period subharmonic oscillations of non-local observables $\{Z_{L_i}\}$ already sharply distinguish our experiment from previous works [13, 34–36, 43], where only local observables break time-translation symmetry, we further demonstrate that the observed Floquet topological order is a nonlocal effect by contrasting with the dynamical behavior of local operators $\{\sigma_k^z\}$. The auto-correlation function $\langle \text{sign}[\sigma_k^z(0)\sigma_k^z(t)] \rangle$ decays to zero quickly without evident oscillations (Fig. 2c), even though the periodic drive is locally applied to each qubit. The striking contrast between nonlocal operators $\{Z_{L_i}\}$ and local operators $\{\sigma_k^z\}$ exposes the locally indistinguishable nature of the Floquet topological order and rules out the possibility of trivial oscillations arising from driving a noninteracting system.

Topologically-ordered Floquet eigenstates

The Floquet eigenstates bear intrinsic topological order and exhibit long-range quantum entanglement characterized by the topological entanglement entropy S_{topo} [17, 18] (see Supplementary Section I.B). To reveal the underlying global entanglement, we prepare an eigenstate of U_F and measure its S_{topo} for different system sizes. In the $B \rightarrow 0$ limit, eigenstates of U_F correspond to superpositions of degenerate eigenstates of H_2 (see Fig. 1b). The eigenstate we prepare is the symmetric superposition of ground states of H_2 , given by $|E_+^{(0)}\rangle = \frac{1}{\sqrt{2}}(|Z_L^{(0)} = 1\rangle + |Z_L^{(0)} = -1\rangle)$. We prepare it from a simple initial product state using a quantum circuit whose depth grows linearly with the system size (see Supplementary Section I.F) [47]:

$$|E_+^{(0)}\rangle = \frac{1}{2^4} (1 + X_L) \prod_q (1 + B_q) |0\rangle^{\otimes 18}. \quad (2)$$

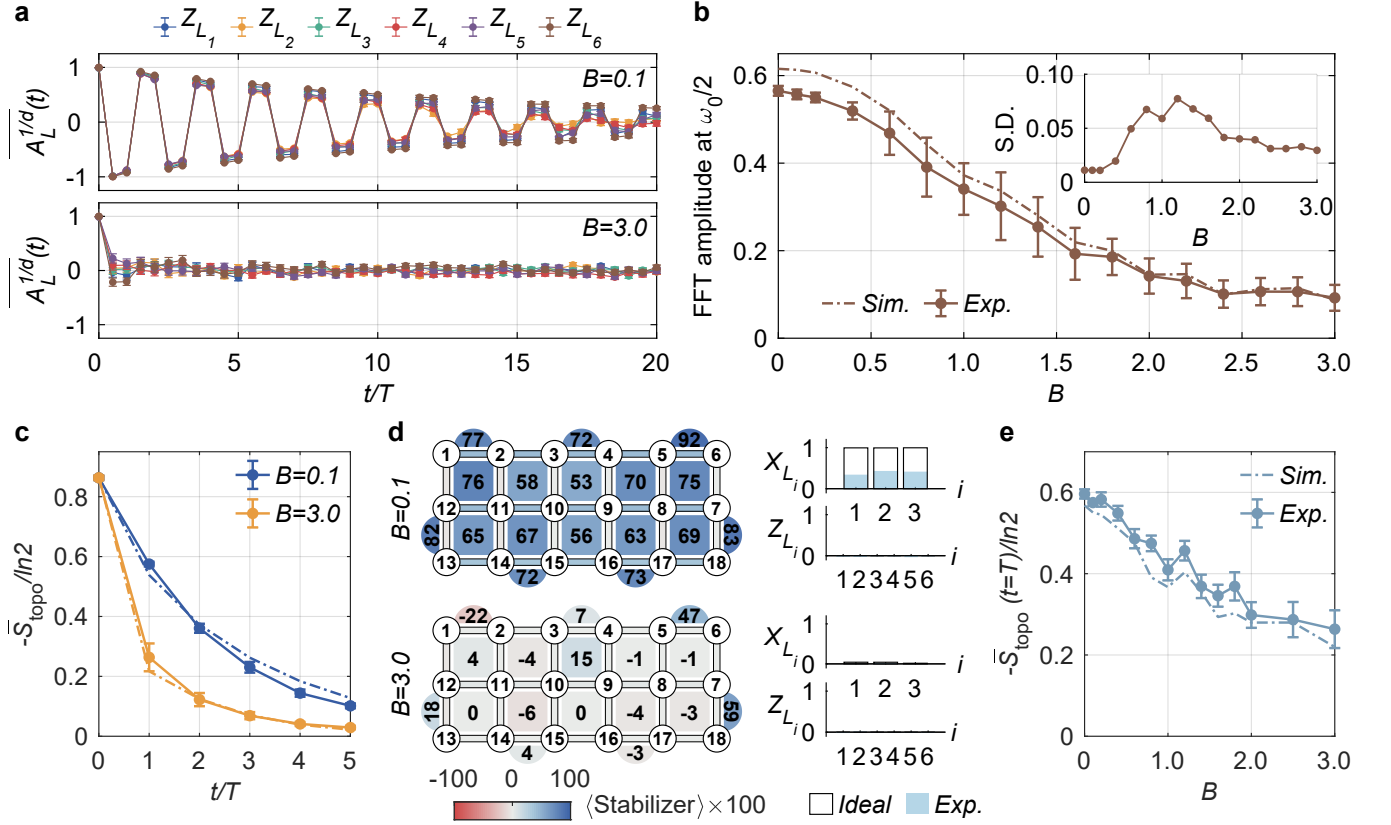


FIG. 4. **Robustness of the topological time-crystalline eigenstate order.** **a**, Measured disorder-averaged auto-correlation function $\overline{A_L^{1/d}(t)}$ for string operators $\{Z_{L_i}\}$ with $B = 0.1$ (upper panel) and $B = 3.0$ (lower panel). Error bars denote the standard error of the statistical mean over 24 random realizations. **b**, Amplitudes of Fourier spectra at $\omega/\omega_0 = 0.5$ as a function of B . Fourier transform of $\overline{A_L^{1/d}(t)}$ is performed using averaged time-domain signals over $\{Z_{L_i}\}$ for up to $t = 6T$. Each data point is averaged over 24 random realizations. Error bars are the standard deviation (S.D.) for 24 disorder realizations. Insert: The S.D. of Fourier spectra amplitudes at $\omega/\omega_0 = 0.5$ as a function of B . **c**, Quench dynamics of the disorder-averaged topological entanglement entropy \bar{S}_{topo} from the initial state $|E_+^{(0)}\rangle$ (which is a Floquet eigenstate at $B = 0$) for different B . Here, $\bar{S}_{\text{topo}}(t \neq 0)$ is obtained by performing state tomography on a four-qubit subsystem and the average is over 12 random realizations; $\bar{S}_{\text{topo}}(t = 0)$ is obtained via the same state tomography process and averaging over five repetitions of eigenstate preparation. **d**, Measured plaquette and string operators for the eigenstate $|E_+^{(0)}\rangle$ after single-step U_F evolution at $B = 0.1$ and $B = 3.0$. **e**, $\bar{S}_{\text{topo}}(t = T)$ as a function of random field strength B , which is averaged over 12 random realizations. Numerical simulations (dashed lines) in **b**, **c**, and **e** are carried out with noisy quantum gates (see Supplementary Section III for details).

We then measure the plaquette operators $\{A_p\}$ and $\{B_q\}$ (left panel of Fig. 3a), and an average value of ~ 0.95 is observed, which is noteworthy given that these operators encode four-body correlations. The high-fidelity gates and long coherence times achieved in our experiment are of crucial importance to obtain such a high average value of the measured stabilizers (see Supplementary Section II.B). We also measure the expectation values of string operators $\{X_{L_i}, Z_{L_i}\}$ and find that $\langle E_+^{(0)} | Z_{L_i} | E_+^{(0)} \rangle \approx 0$ and $\langle E_+^{(0)} | X_{L_i} | E_+^{(0)} \rangle \approx 1$ (right panel of Fig. 3a). These experimental results are in good agreement with theoretical predictions, providing strong evidence that the prepared state is indeed a Floquet eigenstate as desired.

Having prepared the Floquet eigenstate, we further measure its topological entanglement entropy for two different subsystem sizes: four qubits and six qubits. We follow a protocol

developed in Ref. [47] and divide the subsystem into three parts: A, B, and C (upper panels of Fig. 3b). S_{topo} can be extracted from the following combination of von Neumann entanglement entropies [17, 18]:

$$S_{\text{topo}} = S_A + S_B + S_C - S_{AB} - S_{AC} - S_{BC} + S_{ABC}, \quad (3)$$

where S_A is the von Neumann entropy for region A, while AB means the union of regions A and B, and similarly for other terms. For the eigenstates of U_F , the theoretically predicted value of S_{topo} is $-\ln 2$ [17]. For each region i , we perform quantum state tomography on the whole (four-qubit or six-qubit) subsystem and reconstruct ρ_i to calculate the corresponding fidelity $F(\rho_i) = \text{tr} \sqrt{\sqrt{\rho_i} \rho_i^{\text{ideal}} \sqrt{\rho_i}}$ and von Neumann entropy $S_i = -\text{tr}(\rho_i \ln \rho_i)$, where ρ_i^{ideal} is the reduced density matrix of region i obtained by tracing out the complementary region of the ideal Floquet eigenstate. The ex-

perimentally measured S_{topo} , S_i , and $F(\rho_i)$ are shown in the lower panels of Fig. 3b. The measured von Neumann entropy for each region agrees well with the corresponding ideal value. In addition, we observe that $-S_{\text{topo}}/\ln 2$ is 0.86 ± 0.02 for the four-qubit and 0.84 ± 0.08 for the six-qubit subsystem, which is incompatible with the trivial-state value of zero and provides strong evidence for the nontrivial topological nature of the prepared Floquet eigenstate. The deviation between the measured S_{topo} and its corresponding ideal value is due to limited coherence times and gate errors, which is confirmed by numerical results using a noise model estimated via independent measurements (our numerical simulations show that $-S_{\text{topo}}/\ln 2$ is 0.85 and 0.82 for the four-qubit and six-qubit subsystems, respectively; see Supplementary Section III).

Robustness against local perturbations

Topological order is expected to be robust against small local perturbations. In our experiment, we investigate the robustness of the subharmonic response of nonlocal logical operators and of the entanglement dynamics to local perturbations by turning on the random on-site fields in H_1 . We vary the perturbation strength B and measure $\overline{A_{L_i}^{1/d}}(t)$ and $S_{\text{topo}}(t)$, with results plotted in Fig. 4.

Figure 4a shows the measured disorder-averaged autocorrelation function $\overline{A_{L_i}^{1/d}}(t)$ for $\{Z_{L_i}\}$ under weak ($B = 0.1$) and strong ($B = 3.0$) perturbations, which are averaged over 24 realizations with randomly drawn initial states, α_p, β_q , and B_k . With a small perturbation ($B = 0.1$), $\overline{A_{L_i}^{1/d}}(t)$ continues to exhibit persistent subharmonic response up to 20 driving periods (upper panel of Fig. 4a), which is a defining feature of the time-translation symmetry breaking for nonlocal operators and shows the robustness of the observed prethermal topologically ordered discrete time crystal. In contrast, with a strong perturbation ($B = 3.0$), the measured $\overline{A_{L_i}^{1/d}}(t)$ decays quickly to zero and shows no subharmonic response (lower panel of Fig. 4a); at large B , the large onsite field rapidly destroys the topological order preventing any robust period doubling dynamics. To explore the crossover from the time-crystalline to trivial dynamics, we vary the perturbation strength B and Fourier transform the measured time-domain signals. Fig. 4b shows the Fourier amplitudes at $\omega/\omega_0 = 0.5$ with B ranging from 0 to 3.0. We find a small plateau at $B \lesssim 0.25$, which further supports the robustness of the topologically ordered time-crystalline dynamics against weak perturbations. As B increases, the Fourier amplitude decays monotonically and becomes almost flat at $B \gtrsim 2.5$, where the topological order is very quickly destroyed and no period doubling dynamics survives. Sample-to-sample amplitude fluctuations over 24 random realizations (inset of Fig. 4b) display a sharp increase at the same value of B where the Fourier amplitude starts to decay, further highlighting the location of the crossover between the prethermal topological time-crystalline and the trivial dynamics.

We further study the dynamics of the topological entangle-

ment entropy under local perturbations. We first prepare the system in the $B = 0$ Floquet eigenstate $|E_+^{(0)}\rangle$ and then let it evolve under $H(t)$ with varying B . In Fig. 4c, we plot the measured $\overline{S}_{\text{topo}}(t)$ for $B = 0.1$ and $B = 3.0$, respectively. From this figure, we see that $\overline{S}_{\text{topo}}(t)$ drops more quickly at strong perturbation $B = 3.0$ due to the breakdown of the topological phase. We note that $\overline{S}_{\text{topo}}(t)$ also has a slow decay even for $B = 0.1$ due to the accumulated gate errors in the circuit, which is confirmed by the numerical simulations (the dashed lines in Fig. 4c) (see Supplementary Section III). In addition, we measure plaquette and string operators after evolution under U_F for a single time step (see Fig. 4d). From this figure, it is clear that their values are largely preserved for $B = 0.1$, unlike the case of $B = 3.0$, where these values drop to near zero. We further measure the disorder-averaged $\overline{S}_{\text{topo}}(t = T)$ as a function of B (Fig. 4e). Similar to the Fourier spectrum amplitudes in Fig. 4b, $\overline{S}_{\text{topo}}(t = T)$ also decays monotonically with increasing disorder strength. The plateau at weak disorder ($B \lesssim 0.25$) further validates the robustness of time-crystalline dynamics against perturbations.

We note that, for the generic local perturbations considered in our experiment, the overlap between a bare logical operator and its corresponding dressed logical operator may vanish in the thermodynamic limit. This would render the observation of time-crystalline behavior for the bare logical operator infeasible [30]. In addition, to observe the time-crystalline behavior, it is also crucial that $\{\prod \sigma_k^x, Z_L\} = 0$ is satisfied, which requires that the length of Z_L be odd. A possible way to maintain time-crystalline signatures in bare logical operators in the thermodynamic limit and to remove the requirement of odd length Z_L is to consider a surface code with a hole, as discussed in depth in Ref. [30]. In our experiment, we do not adopt such a layout because measuring the corresponding nonlocal logical operator would become very challenging with the current device.

Conclusions and outlook

In summary, we have experimentally observed signatures of a long-lived topologically ordered time crystal in the prethermal regime with a programmable superconducting quantum processor. In contrast to previously reported conventional time crystals, for our observed topologically ordered time crystal, the breaking of discrete time-translation symmetry only occurs for nonlocal logical operators, rather than local observables. We showed persistent subharmonic response for logical operators independent of the initial state and demonstrated robustness of this response to generic perturbations without any microscopic symmetry. In addition, we also prepared a topologically ordered Floquet eigenstate and measured its topological entanglement entropy, which agrees well with theoretical predictions and clearly shows the intrinsic topological nature of the observed time crystal.

The topologically ordered eigenstates of the Floquet unitary are theoretically predicted to exhibit a perimeter law, where the expectation value of a Wilson loop scales with the prime-

ter rather than the area enclosed [30]. In the future, it is desirable to demonstrate such a perimeter law in experiment. The high controllability and programmability of the superconducting processor demonstrated in our experiment also paves the way to exploring a wide range of other exotic non-equilibrium phases with intrinsic topological order that are not accessible in natural materials. In particular, it would be interesting and important to realize various dynamically-enriched topological orders [48]. Indeed, our experiment has demonstrated all necessary building blocks for implementing the Floquet-enriched topological order that hosts dynamical anyon permutation [48] and emergent non-Abelian anyons [49, 50]. An observation of such an unconventional phenomenon would also mark an important step in deepening our understanding of exotic non-equilibrium phases.

Data availability

The data presented in the figures and that support the other findings of this study will be publicly available at Zenodo.org.

Code availability

All the relevant source codes are available from the corresponding authors upon reasonable request.

Acknowledgement The device was fabricated at the Micro-Nano Fabrication Center of Zhejiang University. We acknowledge the support from the Innovation Program for Quantum Science and Technology (Grant Nos. 2021ZD0300200 and 2021ZD0302203), the National Natural Science Foundation of China (Grant Nos. 92065204, 12274368, 12075128, T2225008), and Zhejiang Pioneer (Jianbing) Project (No. 2023C01036). T.I. acknowledges support from the National Science Foundation under Grant No. DMR-2143635. F.M. acknowledges support from the NSF through a grant for ITAMP at Harvard University. A.V.G. was supported in part by the NSF QLCI program (award No. OMA-2120757). N.Y.Y. acknowledges support from the U.S. Department of Energy via the National Quantum Information Science Research Centers Quantum Systems Accelerator and from a Simons Investigator award. W.J., S.J., W.L., Z.L., Z.-Z.S. and D.-L.D. acknowledge in addition support from the Tsinghua University Dushi Program and Shanghai Qi Zhi Institute.

Author contributions L.X. and Z.B. carried out the experiments and analyzed the experimental data under the supervision of Q.G. and H.W.; W.J., L.X., S.J. and Z.B. performed the numerical simulations under the supervision of D.-L.D., Q.G., F.L., F.M., Z.-X.G., A.V.G., and T.I.; D.-L.D., W.J., F.L., F.M., Z.-X.G., A.V.G., N.Y., and T.I. conducted the theoretical analysis; H.L. and J.C. fabricated the device supervised by H.W.; D.-L.D., Q.G., W.J., L.X., H.W., F.L., Z.-X.G., A.V.G., F.M., and T.I. co-wrote the manuscript. All authors contributed to the discussions of the results.

Competing interests All authors declare no competing interests.

* These authors contributed equally

† qguo@zju.edu.cn

‡ hhwang@zju.edu.cn

§ dldeng@tsinghua.edu.cn

- [1] D. C. Tsui, H. L. Stormer, and A. C. Gossard, Two-dimensional magnetotransport in the extreme quantum limit, *Phys. Rev. Lett.* **48**, 1559 (1982).
- [2] X.-G. Wen, Topological orders in rigid states, *Int. J. Mod. Phys. B* **4**, 239 (1990).
- [3] C. Nayak, S. H. Simon, A. Stern, M. Freedman, and S. Das Sarma, Non-abelian anyons and topological quantum computation, *Rev. Mod. Phys.* **80**, 1083 (2008).
- [4] L. D. Landau and E. M. Lifshitz, *Statistical Physics: Volume 5*, Vol. 5 (Elsevier, 2013).
- [5] V. Khemani, A. Lazarides, R. Moessner, and S. L. Sondhi, Phase structure of driven quantum systems, *Phys. Rev. Lett.* **116**, 250401 (2016).
- [6] A. C. Potter, T. Morimoto, and A. Vishwanath, Classification of interacting topological floquet phases in one dimension, *Phys. Rev. X* **6**, 041001 (2016).
- [7] A. Yu. Kitaev, Fault-tolerant quantum computation by anyons, *Ann. Phys.* **303**, 2 (2003).
- [8] X.-G. Wen, Quantum Orders in an Exact Soluble Model, *Phys. Rev. Lett.* **90**, 016803 (2003).
- [9] F. Wilczek, Quantum time crystals, *Phys. Rev. Lett.* **109**, 160401 (2012).
- [10] D. V. Else, B. Bauer, and C. Nayak, Floquet time crystals, *Phys. Rev. Lett.* **117**, 090402 (2016).
- [11] N. Y. Yao, A. C. Potter, I.-D. Potirniche, and A. Vishwanath, Discrete time crystals: Rigidity, criticality, and realizations, *Phys. Rev. Lett.* **118**, 030401 (2017).
- [12] V. Khemani, R. Moessner, and S. L. Sondhi, A Brief History of Time Crystals, *arXiv.1910.10745* (2019).
- [13] X. Zhang, W. Jiang, J. Deng, K. Wang, J. Chen, P. Zhang, W. Ren, H. Dong, S. Xu, Y. Gao, *et al.*, Digital quantum simulation of Floquet symmetry-protected topological phases, *Nature* **607**, 468 (2022).
- [14] R. W. Bomantara, S. Mu, and J. Gong, Topological and dynamical features of periodically driven spin ladders, *Phys. Rev. B* **103**, 235404 (2021).
- [15] A. Chew, D. F. Mross, and J. Alicea, Time-Crystalline Topological Superconductors, *Phys. Rev. Lett.* **124**, 096802 (2020).
- [16] K. Giergiel, A. Dauphin, M. Lewenstein, J. Zakrzewski, and K. Sacha, Topological time crystals, *New J. Phys.* **21**, 052003 (2019).
- [17] A. Kitaev and J. Preskill, Topological Entanglement Entropy, *Phys. Rev. Lett.* **96**, 110404 (2006).
- [18] M. Levin and X.-G. Wen, Detecting topological order in a ground state wave function, *Phys. Rev. Lett.* **96**, 110405 (2006).
- [19] J. Preskill, Quantum Computing in the NISQ era and beyond, *Quantum* **2**, 79 (2018).
- [20] T. I. Andersen, Y. D. Lensky, K. Kechedzhi, I. K. Drozdov, A. Bengtsson, S. Hong, A. Morvan, X. Mi, A. Opremcak, R. Acharya, *et al.*, Non-Abelian braiding of graph vertices in a superconducting processor, *Nature* **618**, 264 (2023).
- [21] S. Xu, Z.-Z. Sun, K. Wang, L. Xiang, Z. Bao, Z. Zhu, F. Shen, Z. Song, P. Zhang, W. Ren, *et al.*, Digital Simulation of Projective Non-Abelian Anyons with 68 Superconducting Qubits, *Chinese Phys. Lett.* **40**, 060301 (2023).
- [22] M. H. Freedman, P/NP, and the quantum field computer, *Proc. Natl. Acad. Sci.* **95**, 98 (1998).

- [23] R. Nandkishore and D. A. Huse, Many-body localization and thermalization in quantum statistical mechanics, *Annu. Rev. Condens. Matter Phys.* **6**, 15 (2015).
- [24] D. A. Abanin, E. Altman, I. Bloch, and M. Serbyn, Colloquium: Many-body localization, thermalization, and entanglement, *Rev. Mod. Phys.* **91**, 021001 (2019).
- [25] T. B. Wahl and B. Béri, Local integrals of motion for topologically ordered many-body localized systems, *Phys. Rev. Res.* **2**, 033099 (2020).
- [26] T. B. Wahl, F. Venn, and B. Béri, Local integrals of motion detection of localization-protected topological order, *Phys. Rev. B* **105**, 144205 (2022).
- [27] D. A. Huse, R. Nandkishore, V. Oganesyan, A. Pal, and S. L. Sondhi, Localization-protected quantum order, *Phys. Rev. B* **88**, 014206 (2013).
- [28] B. Bauer and C. Nayak, Area laws in a many-body localized state and its implications for topological order, *J. Stat. Mech.* **2013**, P09005 (2013).
- [29] Y. Bahri, R. Vosk, E. Altman, and A. Vishwanath, Localization and topology protected quantum coherence at the edge of hot matter, *Nat. Commun.* **6**, 7341 (2015).
- [30] T. B. Wahl, B. Han, and B. Béri, Topologically ordered time crystals, [arXiv:2105.09694](https://arxiv.org/abs/2105.09694) (2021).
- [31] E. V. H. Doggen, I. V. Gornyi, A. D. Mirlin, and D. G. Polyakov, Slow many-body delocalization beyond one dimension, *Phys. Rev. Lett.* **125**, 155701 (2020).
- [32] I.-D. Potirniche, S. Banerjee, and E. Altman, Exploration of the stability of many-body localization in $d > 1$, *Phys. Rev. B* **99**, 205149 (2019).
- [33] W. De Roeck and J. Z. Imbrie, Many-body localization: Stability and instability, *Philos. Trans. R. Soc. Math. Phys. Eng. Sci.* **375**, 20160422 (2017).
- [34] J. Zhang, P. Hess, A. Kyprianidis, P. Becker, A. Lee, J. Smith, G. Pagano, I.-D. Potirniche, A. Potter, A. Vishwanath, *et al.*, Observation of a discrete time crystal, *Nature* **543**, 217 (2017).
- [35] A. Kyprianidis, F. Machado, W. Morong, P. Becker, K. S. Collins, D. V. Else, L. Feng, P. W. Hess, C. Nayak, G. Pagano, *et al.*, Observation of a prethermal discrete time crystal, *Science* **372**, 1192 (2021).
- [36] S. Choi, J. Choi, R. Landig, G. Kucsko, H. Zhou, J. Isoya, F. Jelezko, S. Onoda, H. Sumiya, V. Khemani, *et al.*, Observation of discrete time-crystalline order in a disordered dipolar many-body system, *Nature* **543**, 221 (2017).
- [37] J. Randall, C. E. Bradley, F. V. van der Gronden, A. Galicia, M. H. Abobeih, M. Markham, D. J. Twitchen, F. Machado, N. Y. Yao, and T. H. Taminiau, Many-body-localized discrete time crystal with a programmable spin-based quantum simulator, *Science* **374**, 1474 (2021).
- [38] J. Smits, L. Liao, H. T. C. Stoof, and P. van der Straten, Observation of a Space-Time Crystal in a Superfluid Quantum Gas, *Phys. Rev. Lett.* **121**, 185301 (2018).
- [39] S. Autti, V. B. Eltsov, and G. E. Volovik, Observation of a Time Quasicrystal and Its Transition to a Superfluid Time Crystal, *Phys. Rev. Lett.* **120**, 215301 (2018).
- [40] J. O'Sullivan, O. Lunt, C. W. Zollitsch, M. L. W. Thewalt, J. J. L. Morton, and A. Pal, Signatures of discrete time crystalline order in dissipative spin ensembles, *New J. Phys.* **22**, 085001 (2020).
- [41] S. Pal, N. Nishad, T. S. Mahesh, and G. J. Sreejith, Temporal Order in Periodically Driven Spins in Star-Shaped Clusters, *Phys. Rev. Lett.* **120**, 180602 (2018).
- [42] J. Rovny, R. L. Blum, and S. E. Barrett, Observation of Discrete-Time-Crystal Signatures in an Ordered Dipolar Many-Body System, *Phys. Rev. Lett.* **120**, 180603 (2018).
- [43] X. Mi, M. Ippoliti, C. Quintana, A. Greene, Z. Chen, J. Gross, F. Arute, K. Arya, J. Atalaya, R. Babbush, *et al.*, Time-crystalline eigenstate order on a quantum processor, *Nature* **601**, 531 (2022).
- [44] C. Ying, Q. Guo, S. Li, M. Gong, X.-H. Deng, F. Chen, C. Zha, Y. Ye, C. Wang, Q. Zhu, *et al.*, Floquet prethermal phase protected by U(1) symmetry on a superconducting quantum processor, *Phys. Rev. A* **105**, 012418 (2022).
- [45] Z. Lu, P.-X. Shen, and D.-L. Deng, Markovian Quantum Neuroevolution for Machine Learning, *Phys. Rev. Appl.* **16**, 044039 (2021).
- [46] R. W. Bomantara, Nonlocal discrete time crystals in periodically driven surface codes, *Phys. Rev. B* **104**, 064302 (2021).
- [47] K. J. Satzinger, Y.-J. Liu, A. Smith, C. Knapp, M. Newman, C. Jones, Z. Chen, C. Quintana, X. Mi, A. Dunsworth, *et al.*, Realizing topologically ordered states on a quantum processor, *Science* **374**, 1237 (2021).
- [48] A. C. Potter and T. Morimoto, Dynamically enriched topological orders in driven two-dimensional systems, *Phys. Rev. B* **95**, 155126 (2017).
- [49] J. R. Wootton, V. Lahtinen, Z. Wang, and J. K. Pachos, Non-abelian statistics from an abelian model, *Phys. Rev. B* **78**, 161102 (2008).
- [50] M. Kalinowski, N. Maskara, and M. D. Lukin, Non-Abelian Floquet Spin Liquids in a Digital Rydberg Simulator, *Phys. Rev. X* **13**, 031008 (2023).

Supplementary Information: Long-lived topological time-crystalline order on a quantum processor

CONTENTS

I. Theoretical analysis	1
A. Surface-code model	1
B. Topological order of the surface-code model	2
C. Topological time-crystalline order	3
D. Stability of topological time-crystalline order	5
E. Quantum circuits for the Floquet unitary	6
F. Floquet eigenstate preparation circuits	7
II. Experimental information	8
A. Experimental platform	8
B. System calibration	9
C. Microwave crosstalk	10
D. Flux-bias crosstalk	10
E. Device-aware circuit transformation	10
III. Numerical simulations	13
A. Error model and noisy simulation	14
References	15

I. THEORETICAL ANALYSIS

In this work, we experimentally observe topological time-crystalline order, which can be characterized by the subharmonic temporal response of nonlocal logical operators [S1, S2]. The topological time-crystalline order is realized in a periodically driven surface-code model. In this section, we will first briefly introduce the topological properties of the surface code and provide theoretical analysis of the emergence of topological time-crystalline order. Then, we will show how to use a set of elementary quantum gates to implement the Floquet unitary and to prepare the Floquet eigenstates with a programmable superconducting quantum processor.

A. Surface-code model

Recent progress [S1, S3, S4] has demonstrated that many physical systems and their properties can be described using the language of topology; an important example of this is topological stabilizer codes [S5]. The surface-code model is an important

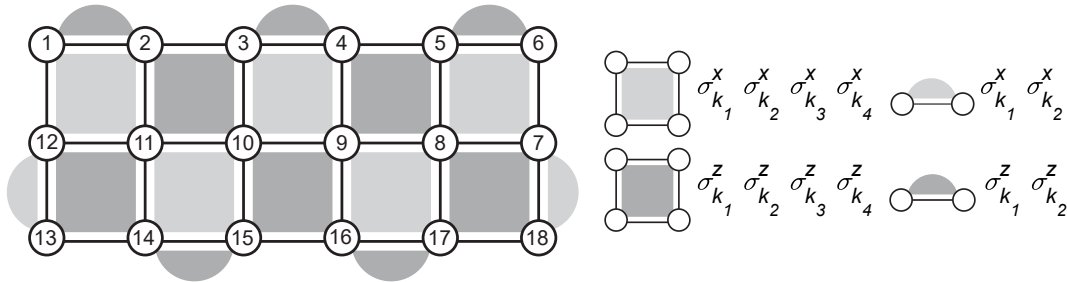


FIG. S1. **The layout of a 3×6 rotated surface-code model.** Circles represent qubits. The shaded plaquettes and semicircles indicate the local four-body and two-body operators on connected qubits, respectively. The dark (light) gray regions represent the A_p (B_q) plaquette operators.

topological stabilizer code that has numerous applications in quantum error correction [S6–S9]. It is analytically solvable and is also of interest to researchers from other fields, including condensed matter physics.

We adapt a variant of the surface-code model: the rotated surface code defined on a planar lattice with open boundary conditions [S10] (see Fig. S1). Its Hamiltonian is given by

$$H = - \sum_p \alpha_p A_p - \sum_q \beta_q B_q, \text{ with } A_p = \prod_{k \in p} \sigma_k^z \text{ and } B_q = \prod_{k \in q} \sigma_k^x, \quad (\text{S1})$$

where the plaquettes p and q are shown in Fig. S1, and α_p, β_q are randomly chosen positive coefficients. For simplicity, unless otherwise specified, we do not distinguish the plaquette operators and the semicircle operators in the following discussions. We note that A_p, B_q are both Pauli strings and have eigenvalues ± 1 . String operators consisting of the same type of Pauli operators commute with each other: $[A_p, A_{p'}] = [B_q, B_{q'}] = 0$. Additionally, A_p and B_q also mutually commute because the overlap between the support of A_p and any B_q has an even number of qubits. We conclude that the ground states of the rotated surface-code model are simultaneous eigenstates of all plaquette operators A_p and B_q with eigenvalue $+1$. Furthermore, each excited eigenstate of the Hamiltonian is a simultaneous eigenstate of all plaquette operators with different eigenvalues. The model in Fig. S1 has 18 physical qubits and 17 independent plaquette operators, and the remaining single-qubit degree of freedom leads to a two-fold degeneracy for each energy level.

Suppose $|\psi\rangle$ is one of the ground states of H defined on the lattice shown in Fig. S1. That is, all plaquette operators have an expectation value of 1: $\langle \psi | A_p | \psi \rangle = \langle \psi | B_q | \psi \rangle = +1$ for arbitrary plaquettes p, q . To find another ground state, we try to flip the qubit with index $k = 1$. However, this changes the sign of the expectation value of at least one of the plaquette operators, such as the one supported by qubits 1 and 2, i.e. $\langle \psi | \sigma_1^x A_{\{1,2\}} \sigma_1^x | \psi \rangle = -1$. Thus, the state with one flipped spin is no longer a ground state. To maintain the sign of $\langle A_{\{1,2\}} \rangle$, we flip qubit 2, but this changes the signs of other connected plaquette operators. Thus we are forced to continue this process until qubits $k = 1, \dots, 6$ are all flipped. The final state is then still a simultaneous $+1$ eigenstate of all plaquette operators, since the string flip operator commutes with all plaquette operators: $[\prod_{k=1}^6 \sigma_k^x, A_p] = [\prod_{k=1}^6 \sigma_k^x, B_q] = 0$. We denote the string operator by $X_L \equiv \prod_{k=1}^6 \sigma_k^x$. It cannot be represented as a product of any combination of plaquette operators. Similarly, we can also define $Z_L \equiv \prod_{k=1,12,13} \sigma_k^z$, which anticommutes with X_L . This defines a Pauli algebra on a single logical qubit, and we conclude that the ground state manifold has a two-fold degeneracy indexed by, e.g., $\langle Z_L \rangle = \pm 1$. The same analysis can also be applied to any excited eigenstate. For the l -th energy level, we denote the eigenstates satisfying $\langle Z_L \rangle = \pm 1$ by $|Z_L^{(l)}\rangle = \pm 1$. In the topological stabilizer formalism, plaquette operators are called stabilizers, and the ground space is called the code space, which is manipulated by logical string operators X_L, Z_L .

B. Topological order of the surface-code model

In the language of group theory, we can define a group generated by the plaquette operators (stabilizers) $S = \langle A_p, B_q \rangle$, and an 18-qubit Pauli group $P_{18} = \langle \sigma_k^x, \sigma_k^z : k \text{ runs over all sites} \rangle$. S is a subgroup of P_{18} . The centralizer group $C_{P_{18}}(S)$ consists of all operators in P_{18} that simultaneously commute with all plaquette operators. For the rotated surface-code model, S is a normal subgroup of $C_{P_{18}}(S)$ and we have the quotient group $C_{P_{18}}(S)/S \cong P_1$ being the Pauli group for one qubit. The above discussion indicates that the two-fold degeneracy of each eigenstate of Eq. (S1), discussed in the previous section, is directly related to the topology of the system. Any single-qubit operator fails to commute with at least one plaquette operator. According to the discussion in Section I.A, we know that Z_L and X_L are two independent nonlocal operators which can map one eigenstate to its degenerate partner. As a consequence, they can be regarded as the representatives of the cosets of S . Since arbitrary products of the plaquette operators with Z_L (X_L) are equivalent to Z_L (X_L) itself in a fixed stabilizer eigenspace, we have several equivalent expressions for operators Z_L and X_L (see Fig. 2 of the main text): $Z_{L_1} = \prod_{k=1,12,13} \sigma_k^z, Z_{L_2} = \prod_{k=2,11,14} \sigma_k^z, \dots$ and $X_{L_1} = \prod_{k=1}^6 \sigma_k^x, X_{L_2} = \prod_{k=7}^{12} \sigma_k^x, \dots$, all of which are nonlocal operators. All operators within each coset are equivalent modulo S .

A connection between topological order and quantum entanglement is provided by the topological entanglement entropy. For a many-body wavefunction, the von Neumann entropy of a subregion, $S(\rho_{\text{sub}}) \equiv -\text{tr} \rho_{\text{sub}} \ln \rho_{\text{sub}}$, describes the quantum entanglement between the subregion and its complement. Here, ρ_{sub} denotes the reduced density matrix of the subregion obtained by tracing out the complementary region. For a system obeying the entanglement area law, the von Neumann entropy of a subregion is represented as [S11]

$$S(\rho_{\text{sub}}) = \alpha \partial_{\text{sub}} - \gamma + \dots \quad (\text{S2})$$

Here, α is a constant determined by the details of the system, ∂_{sub} is the volume of the subregion's boundary, and $-\gamma$ is the topological entanglement entropy, which characterizes nonlocal entanglement persisting at arbitrarily large distances. In topological quantum field theory, it is known that $\gamma = \ln \mathcal{D}$, where \mathcal{D} is the total quantum dimension [S11]. In an Abelian anyon model, \mathcal{D} is the square root of the number of superselection sectors corresponding to inequivalent quasi-particle species. For

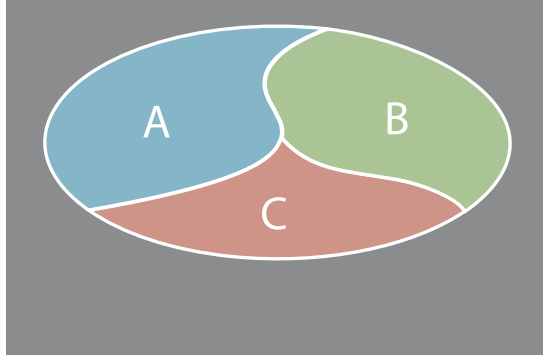


FIG. S2. Regions A , B , and C defined for computing topological entanglement entropy via Eq. (S3).

the rotated surface-code model, there are two types of Abelian anyons: electric charges e associated with A_p plaquette operators and magnetic charges m associated with B_q plaquette operators. So, there are four quasi-particle sectors (identity, e , m , and em) and the total quantum dimension \mathcal{D} is equal to $\sqrt{4} = 2$. Thus, the topological entanglement entropy $S_{\text{topo}} = -\ln 2$ for the model (S1). To measure S_{topo} , we cancel out boundary contributions by dividing the subregion into three parts that are all large compared to the correlation length [S11] (see Fig. S2) and computing

$$S_{\text{topo}} = S_A + S_B + S_C - S_{AB} - S_{BC} - S_{AC} + S_{ABC}, \quad (\text{S3})$$

where S_A is the von Neumann entropy of region A , S_{AB} is the von Neumann entropy of region $A \cup B$, and so on. In this way, all boundary terms are canceled out, and the result is the topological entanglement entropy $S_{\text{topo}} = -\gamma$.

C. Topological time-crystalline order

Having reviewed the concept of topological order in the static rotated surface-code model, we now generalize to the periodically driven setting and show the emergence of topological time-crystalline order. The Floquet Hamiltonian of the driven rotated surface-code model is

$$\begin{aligned} H(t) &= \begin{cases} H_1, & 0 \leq t < T', \\ H_2, & T' \leq t < T, \end{cases} \\ H_1 &\equiv \frac{\pi}{2} \sum_k \sigma_k^x + \sum_k \mathbf{B}_k \cdot \boldsymbol{\sigma}_k, \\ H_2 &\equiv -\sum_p \alpha_p A_p - \sum_q \beta_q B_q, \end{aligned} \quad (\text{S4})$$

where \mathbf{B}_k is an on-site field randomly chosen from a ball with radius B , $\boldsymbol{\sigma}_k$ is the vector of Pauli operators, A_p, B_q are plaquette operators defined in Fig. S1, α_p, β_q are coefficients uniformly chosen from $[0, 2\pi)$, and $T = 2T' = 2$. H_2 is the rotated surface-code Hamiltonian, and its spectrum is exactly two-fold degenerate, with eigenstates $|Z_L^{(l)} = \pm 1\rangle$ at energy ϵ_l . These two-fold degenerate eigenstates cannot be distinguished by any local operator. However, they can be distinguished by a nonlocal string operator such as Z_L . When $B = 0$, the effect of $U_1 = e^{-i\pi/2 \sum_k \sigma_k^x} \propto \prod_k \sigma_k^x$ is to flip all the qubits. When we index degenerate eigenstates of H_2 with a logical operator Z_L of odd length, this is equivalent to applying a logical operator X_L . In this situation, we have the relations

$$U_F |Z_L^{(l)} = 1\rangle = \exp(-i\epsilon_l) |Z_L^{(l)} = -1\rangle, \quad U_F |Z_L^{(l)} = -1\rangle = \exp(-i\epsilon_l) |Z_L^{(l)} = 1\rangle, \quad (\text{S5})$$

where $U_F = \exp(-iH_2) \exp(-iH_1)$ is the Floquet unitary. In other words, U_F toggles between two degenerate eigenstates of H_2 . In a degenerate eigenspace of H_2 , U_F can thus be represented as a matrix

$$U_F \sim \begin{bmatrix} 0 & \exp(-i\epsilon_l) \\ \exp(-i\epsilon_l) & 0 \end{bmatrix}. \quad (\text{S6})$$

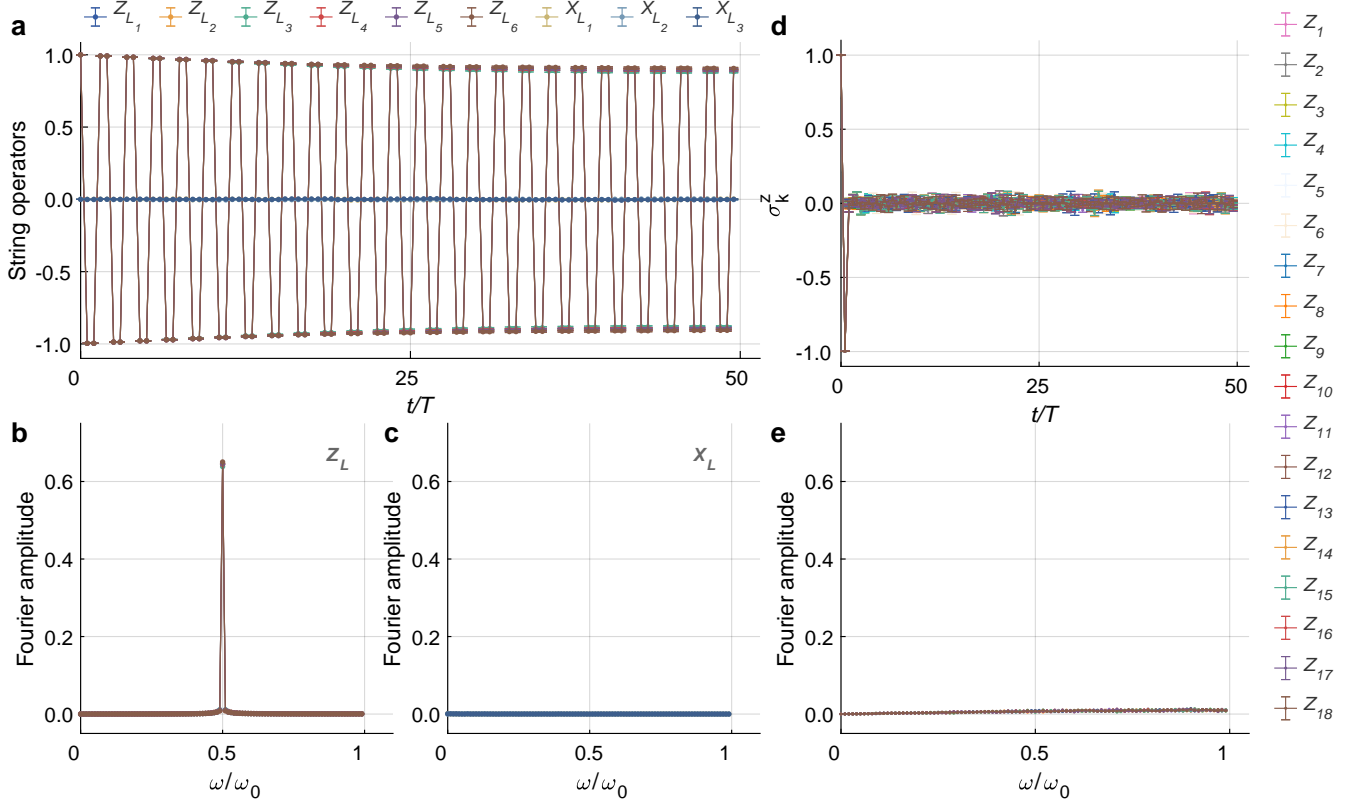


FIG. S3. **Dynamics of nonlocal and local observables at $B = 0.1$.** All data in this figure are averaged over 1000 random realizations, and the error bars stand for the standard error of the statistical mean. **a**, Disorder-averaged dynamics of nonlocal string operators $\{Z_{L_i}\}$ and $\{X_{L_i}\}$. Expectation values of all six $\{Z_{L_i}\}$ lying on top of each other, break the time-translation symmetry, and manifest subharmonic oscillations with period $2T$. Despite the initial slight decay, mainly caused by the imperfect overlap between the dressed logical operators and the measured bare operators, the $\{Z_{L_i}\}$ expectation values show a plateau at late times, indicating persistent oscillations. In contrast, expectation values of all three $\{X_{L_i}\}$ (lie on top of each other) remain zero as expected. **b**, The Fourier spectrum of the disorder-averaged dynamics of $\{Z_{L_i}\}$. The peaks at $\omega/\omega_0 = 1/2$ ($\omega_0 = 2\pi/T$) indicate the subharmonic oscillations of $\{Z_{L_i}\}$. **c**, The Fourier spectrum of the disorder-averaged dynamics of $\{X_{L_i}\}$. **d**, Disorder-averaged dynamics of single-qubit operators $\{\sigma_k^z\}$. **e**, The Fourier spectrum of the disorder-averaged dynamics of single-qubit operators $\{\sigma_k^z\}$.

Therefore, in this eigenspace, U_F has eigenvalues $\pm \exp(-i\epsilon_l)$ corresponding to Floquet eigenstates $|E_{\pm}^{(l)}\rangle \propto |Z_L^{(l)} = 1\rangle \pm |Z_L^{(l)} = -1\rangle$, respectively. For the Floquet Hamiltonian $H_F = i \log U_F$, the corresponding quasi-energies are ϵ_l and $\epsilon_l + \pi$ (see Fig. 1b of the main text). We note that the H_2 eigenstates $|Z_L^{(l)} = 1\rangle$ and $|Z_L^{(l)} = -1\rangle$ have the same topological entanglement entropy $S_{\text{topo}} = -\ln 2$, which is the core feature of the topological order of this model. The Floquet eigenstates $|E_{\pm}^{(l)}\rangle$ inherit the same value of S_{topo} .

We further investigate the dynamical behavior of the nonlocal string operators. Without loss of generality, we start from a product state $|\psi_0\rangle$ which has expectation value of $+1$ for the string operator Z_L , such as $|\psi_0\rangle = \bigotimes_k |0\rangle_k$. This can be represented as a superposition of the subset of eigenstates $\{|Z_L^{(l)} = 1\rangle\}$: $|\psi_0\rangle = \sum_l \alpha_l |Z_L^{(l)} = 1\rangle$, such that $\langle \psi_0 | Z_L | \psi_0 \rangle = \sum_{l'l'} \alpha_{l'}^* \alpha_l \langle Z_L^{(l')} = 1 | Z_L | Z_L^{(l)} = 1 \rangle = \sum_{l'l} \alpha_{l'}^* \alpha_l \delta_{l'l} = 1$. Under time evolution by the Floquet unitary U_F , we find that

$$\begin{aligned}
 U_F |\psi_0\rangle &= \exp(-iH_2) \exp(-iH_1) \sum_l \alpha_l |Z_L^{(l)} = 1\rangle \\
 &= \exp(-iH_2) \sum_l \alpha_l |Z_L^{(l)} = -1\rangle \\
 &= \sum_l \alpha_l e^{i\epsilon_l} |Z_L^{(l)} = -1\rangle \\
 &\equiv |\psi_1\rangle.
 \end{aligned} \tag{S7}$$

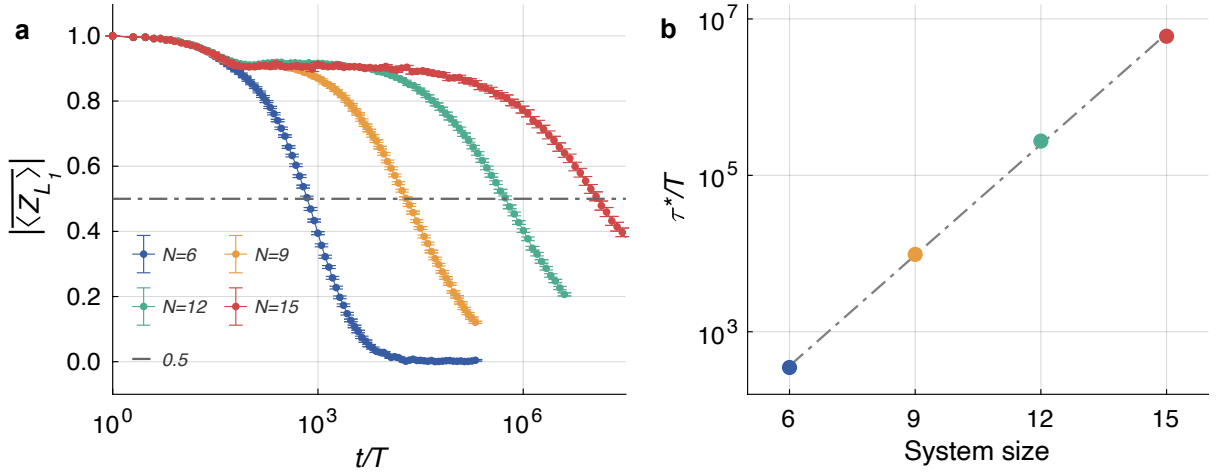


FIG. S4. **Lifetime of the topological time-crystalline order.** Experimentally measuring the lifetime of the topological time-crystalline order is infeasible due to the limited coherence time of our experimental device. **a**, Disorder-averaged dynamics of the nonlocal logical qubit expectation values $|\langle \psi_n | Z_{L_1} | \psi_n \rangle|$ (we first take the average, and then take the absolute value). The results are averaged over a number of random realizations ranging from 10^3 ($N = 15$) to 10^4 ($N = 6$) depending on the system size. The results show that, after an initial slight decay, $|\langle \psi_n | Z_{L_1} | \psi_n \rangle|$ reaches a plateau extending up to a timescale that diverges exponentially with the system size (see panel **b**). The gray dashed line indicates the reference value of $1/2$ that is used to extract the logical-qubit lifetime. Error bars represent the standard error of the statistical mean. **b**, Finite-size scaling of the lifetime of the topological time-crystalline order. The colored dots exhibit the exponential scaling of τ^*/T with system size, where τ^* is the time at which $|\langle \psi_n | Z_{L_1} | \psi_n \rangle|$ reaches $1/2$. The gray dashed line is a best-fit exponential for the system-size dependence of τ^*/T .

If we measure the string operator Z_L after a single Floquet period T , we have

$$\langle \psi_1 | Z_L | \psi_1 \rangle = \sum_{l'l} \alpha_{l'}^* \alpha_l e^{-i(\epsilon_l - \epsilon_{l'})} \langle Z_L^{(l')} = -1 | Z_L | Z_L^{(l)} = -1 \rangle = - \sum_{l'l} \alpha_{l'}^* \alpha_l e^{-i(\epsilon_l - \epsilon_{l'})} \delta_{l'l} = -1. \quad (\text{S8})$$

Similarly, the stroboscopic dynamics of the string operator Z_L after a time $t = nT$ is $\langle \psi_n | Z_L | \psi_n \rangle = (-1)^n$, where $|\psi_n\rangle = (U_F)^n |\psi_0\rangle$. Therefore, the expectation values of Z_L oscillate with period $2T$, which breaks the discrete time-translation symmetry of the Floquet Hamiltonian (S4). The corresponding numerical simulations are shown in Fig. S3a, b. For the string operator X_L , one can check that $\langle \psi_n | X_L | \psi_n \rangle = 0$ (see Fig. S3a, c).

In contrast, we find that local operators exhibit featureless dynamics in our Floquet model. For a single-qubit operator O_{single} , we have

$$\langle \psi_0 | O_{\text{single}} | \psi_0 \rangle = \sum_{l'l} \alpha_{l'}^* \alpha_l \langle Z_L^{(l')} = 1 | O_{\text{single}} | Z_L^{(l)} = 1 \rangle, \quad (\text{S9})$$

and

$$\langle \psi_1 | O_{\text{single}} | \psi_1 \rangle = \sum_{l'l} \alpha_{l'}^* \alpha_l e^{-i(\epsilon_l - \epsilon_{l'})} \langle Z_L^{(l')} = -1 | O_{\text{single}} | Z_L^{(l)} = -1 \rangle. \quad (\text{S10})$$

The extra phase factors $e^{-i(\epsilon_l - \epsilon_{l'})}$ tend to be randomly distributed under the Floquet dynamics of Hamiltonian (S4), leading to a fast decay to zero for $\langle \psi_n | O_{\text{single}} | \psi_n \rangle$ (see Fig. S3d, e) and thus to an impossibility of time-translation symmetry breaking. This distinction between the dynamics of local and nonlocal operators is the key difference between the topological time-crystalline order and conventional time-crystalline order.

D. Stability of topological time-crystalline order

The stability of the topological time-crystalline order is a highly non-trivial problem and is still open for further exploration. For example, it is believed that many-body localization (MBL) can help prevent a Floquet system from heating to infinite temperature. However, the stability of MBL in the thermodynamic limit is still controversial [S12–S14] (especially in two or

more spatial dimensions), and investigating such open problems is beyond the scope of the present work. Here, we perform a preliminary numerical simulation to explore the stability of the topological time-crystalline order against small local random fields.

In our numerical simulations, we define the lifetime as the number of Floquet periods elapsed before the magnitude of the expectation value of Z_L decays to $1/2$. We fix a small perturbation strength $B = 0.1$ for this study. In the presence of random on-site fields, the contribution of H_1 to the Floquet unitary is no longer a perfect spin-flip operator for all the sites; rather, it is

$$U_1 = e^{-iH_1} \sim \prod_k \sigma_k^x + O(B). \quad (\text{S11})$$

As the underlying lattice structure can have a significant effect on the lifetime of the logical qubit, we carry out the numerical simulations for lattices of dimensions $3 \times 2, 3 \times 3, 3 \times 4, 3 \times 5$, and measure the non-local logical Z operator of fixed length 3. The initial states are randomly chosen z -basis product states in order to give definite expectation values of ± 1 for the string operator Z_L . For each realization, we numerically calculate the dynamics under Eq. (S4) for a long enough time to observe the decay of the string operator. The final results are averaged over many such random realizations, and the time at which the expectation values reach $1/2$ is regarded as the indicator of the lifetime (see Fig. S4a). Our results show that the lifetime of the topological order for the model is much longer than any experimentally accessible timescale. Furthermore, we observe that the lifetime of the logical qubit grows exponentially with system size for $N = 6, 9, 12, 15$ (see Fig. S4b). We conclude that, owing to disorder, the true thermalization time is much larger than these experimentally inaccessible timescales, and thus the observed topological time crystalline behavior is robust.

E. Quantum circuits for the Floquet unitary

It is straightforward to realize the Floquet drive $U_1(t) = e^{-itH_1}$ with tensor products of single-qubit rotations, which can be represented via Euler angles (see Fig. S5a). However, the circuit construction of $U_2(t) = e^{-itH_2}$ is more challenging due to the four-body plaquette operators A_p, B_q in the Hamiltonian H_2 . To construct digital quantum circuits for this evolution, we exploit the property that all plaquette operators mutually commute, so that the evolution reads

$$U_2(t) = e^{-itH_2} = \prod_p e^{it\alpha_p A_p} \prod_q e^{it\beta_q B_q}. \quad (\text{S12})$$

Besides, we have the relation $H\sigma^z H = \sigma^x$, where H is the single-qubit Hadamard gate. Thus, for any plaquette q , we have

$$H^{\otimes q} (e^{it\beta_q B_q}) H^{\otimes q} = e^{it\beta_q A_q}, \quad (\text{S13})$$

where $H^{\otimes q}$ stands for a Hadamard transform applied to the qubits in plaquette q . Therefore, the circuit construction for evolution under H_2 reduces to simulating a single plaquette operator A_p .

Variational quantum circuits are a powerful tool for NISQ quantum computation and quantum simulation and have been intensively studied in recent years [S15, S16]. We adapt this method to construct the quantum circuit for evolution under the plaquette operator A_p . Variational quantum circuits are composed of gates with parameterized rotation angles that can be updated according to various algorithms. The circuit construction for the evolution operator of A_p can be divided into two steps. First, we need to find an appropriate variational ansatz for it. Second, we optimize the variational parameters in this ansatz to minimize the distance between the corresponding quantum circuit and the target unitary.

For the first step, we use the neuroevolution method [S17] to find a suitable variational quantum circuit architecture. The complete gate set used in our experiment consists of three kinds of single-qubit rotations $X(\theta), Y(\theta), Z(\theta)$ and a controlled-phase gate $\text{CR}_z(\theta)$ along the z axis (θ stands for the variational parameter). Then, we can construct a directed graph where each node represents a block of gates that can be implemented in parallel, and where the directed edges denote allowed sequences of blocks. A quantum circuit can then be represented as a directed path in this graph. To find a desired circuit ansatz, we use the following procedure:

1. Randomly sample several paths with a fixed depth in the constructed directed graph as our initial quantum-circuit ansatz;
2. For each path representing an ansatz, minimize the cost function $L(\boldsymbol{\theta})$, which is given by

$$L(\boldsymbol{\theta}) = 1 - \text{Tr} \left[U_{\text{target}}^\dagger U_{\text{circuit}}(\boldsymbol{\theta}) \right] / d, \quad (\text{S14})$$

where U_{target} is the evolution unitary of the plaquette operator A_p , U_{circuit} is the unitary represented by the current quantum-circuit ansatz with variational parameters $\boldsymbol{\theta}$, and d is the dimension of the Hilbert space. $L(\boldsymbol{\theta})$ measures the distance between the target unitary and the current quantum circuit. We update variational parameters using gradient-based algorithms;

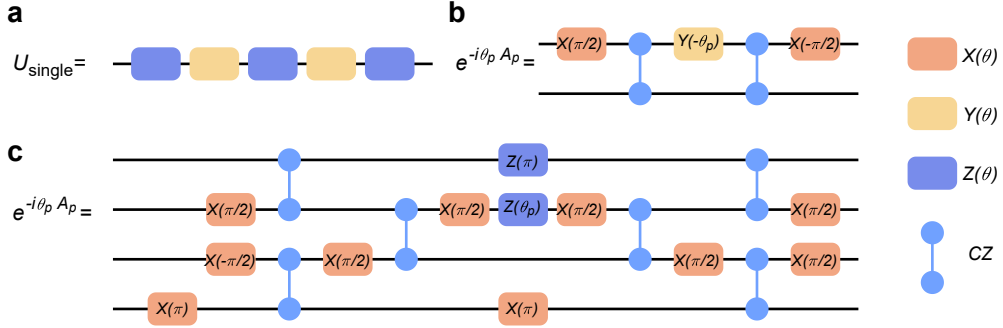


FIG. S5. **Digital quantum circuits for the Floquet unitary.** (a) Single-qubit circuit realizing U_1 . We use Euler angles to represent general single-qubit rotations. (b) Circuit realizing the evolution unitary of the two-body plaquette A_p on the boundary of the lattice (see Fig. S1). (c) Circuit realizing the evolution unitary of the four-body plaquette A_p . Combining these elementary circuits allows us to digitally simulate the Hamiltonian (S4). In experiments, the whole circuit is further compiled to reduce the depth.

3. Keep the ansatz with smallest values of the loss function $L(\theta)$, and prolong the corresponding paths in the directed graph to generate new circuits with larger depth;
4. Iterate steps 2 and 3 until the loss function converges.

We repeat this algorithm several times and choose the circuit ansatz with the smallest value of the loss function as the optimal result.

Remarkably, in some cases, we can obtain ansatz circuits with an extremely small distance from our target unitary (typically, the loss function $L(\theta) < 10^{-4}$), which indicates that there probably exists a circuit ansatz that is analytically equivalent to the target unitary. Thus, we further manually simplify the obtained variational circuit ansatz. Precisely speaking, we alternately utilize the following methods to reduce the number of the variational parameters in this ansatz:

1. Drop those gates very close to the identity gate, i.e., variational gates with small rotation angles.
2. Fix those gates with special parameters, such as $\theta = \pi$.
3. Change the order of some commuting gates.
4. Split or combine some neighboring gates.

After the reduction process above, we obtain an experimentally friendly circuit that analytically represents the evolution unitary $U(t) = e^{it\alpha_p A_p}$ (see Fig. S5b, c). The evolution unitary of B_q is then obtained by inserting a layer of Hadamard gates before and after $U(t)$. Then, we can obtain the digital quantum circuit for U_2 by concatenating the evolution operators for all plaquette operators. This yields an analytical representation of the whole time-evolution unitary (see Fig. 1 of the main text).

F. Floquet eigenstate preparation circuits

In the main text, we experimentally measure the topological entanglement entropy of a Floquet eigenstate. Here, we provide more details on the circuit for preparing this state. In our model, the Floquet eigenstates $|E_{\pm}^{(l)}\rangle \propto |Z_L^{(l)} = 1\rangle \pm |Z_L^{(l)} = -1\rangle$ are superpositions of the eigenstates ($|Z_L^{(l)} = \pm 1\rangle$) of the rotated surface-code Hamiltonian. We follow the method in Ref. [S18] to realize the eigenstates $|Z_L^{(l)} = \pm 1\rangle$ and their superpositions. Here, we briefly summarize the idea of this method.

Without loss of generality, we choose the Floquet eigenstate that superposes the two-fold degenerate ground states of H_2 . Because the ground states are the simultaneous eigenstates of all plaquette operators, we can apply the projector $\prod_{p,q} (\mathbb{1} + A_p)(\mathbb{1} + B_q)$ to map the initial state into the ground space. For simplicity, we choose an initial state of $|0\rangle^{\otimes 18}$. The projector above is a sequence of mutually commuting projection operators, which project the initial state into a simultaneous eigenstate of A_p and B_q . The final state is unchanged after exchanging the order of the projection operators, since $[A_p, B_q] = 0$. Since $(\mathbb{1} + A_p)|0\rangle^{\otimes 18} = |0\rangle^{\otimes 18}$, we conclude that $|Z_L^{(0)} = 1\rangle \propto \prod_q (\mathbb{1} + B_q)|0\rangle^{\otimes 18}$ (ignoring an overall normalization factor). Furthermore, since $|Z_L^{(0)} = -1\rangle = X_L|Z_L^{(0)} = 1\rangle$, we can express the superposition of ground states in two topological sectors

as $|Z_L^{(0)} = 1\rangle + |Z_L^{(0)} = -1\rangle \propto (\mathbb{1} + X_L) \prod_q (\mathbb{1} + B_q) |0\rangle^{\otimes 18}$. Since B_q only consists of σ^x operators, we have $[X_L, B_q] = 0$. As a result, we can also write $|Z_L^{(0)} = 1\rangle + |Z_L^{(0)} = -1\rangle \propto \prod_q (\mathbb{1} + B_q) (\mathbb{1} + X_L) |0\rangle^{\otimes 18}$.

Since all the X_{L_k} are equivalent in our model, we fix $X_L = \prod_{k=7}^{12} \sigma_k^x$ in the following discussion. We first show how to prepare the state $(\mathbb{1} + X_L) |0\rangle^{\otimes 18}$. The effect of $\mathbb{1} + X_L$ is to project the initial zero state into a cat state of the form $(|000000\rangle + |111111\rangle)_{7,\dots,12} \otimes |0\rangle^{\otimes 12}$. This cat state can be prepared conveniently with quantum gates by first applying a Hadamard gate on one of the qubits in $\{7, \dots, 12\}$ and then successively applying CNOT gates for each pair of neighboring qubits. The effect of the projection operators $\mathbb{1} + B_q$ can be realized by applying similar gate sequences to the qubits in plaquette q .

II. EXPERIMENTAL INFORMATION

Exploring an intrinsically non-equilibrium Floquet system [Eq. (S4)] relies on the dynamical manipulation of highly entangled many-body states. In our work, we engineer a topological “synthetic quantum material” on a 3×6 superconducting qubit lattice using the digital quantum simulation paradigm. In this section, we provide detailed information on the experimental platform, device performance, and circuit calibration.

A. Experimental platform

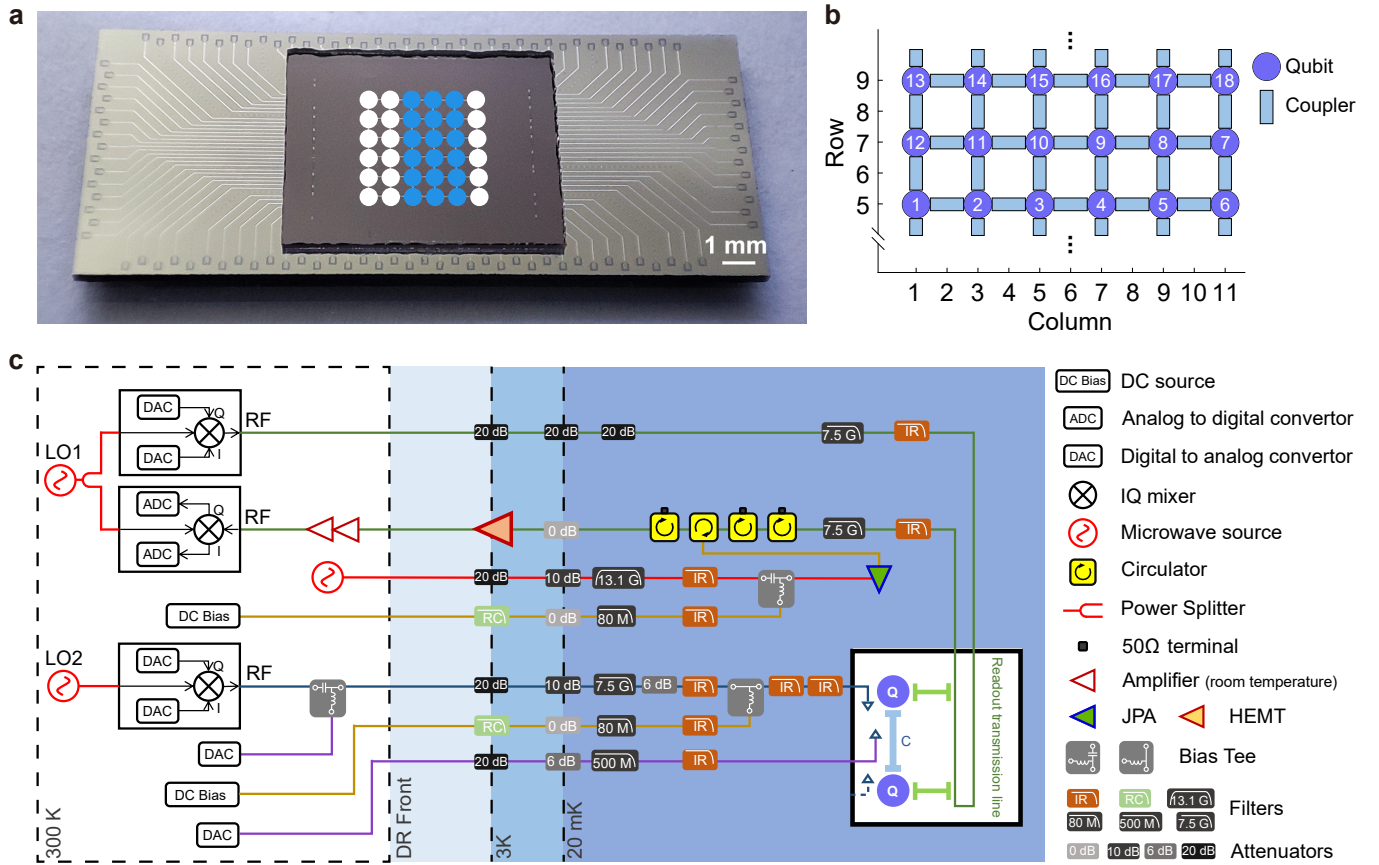


FIG. S6. **Quantum processor and experimental setup.** **a**, Photo of the flip-chip quantum processor. The 18 qubits actively used in our experiments are marked by blue solid circles, while the other unused qubits are marked by white circles. **b**, Schematic structure of the 3×6 qubit lattice. Qubits are arranged at the vertices of a 3×6 grid, and couplers are represented by the edges. **c**, Wiring information. The superconducting quantum chip is mounted on the mixing chamber plate (20 mK) of the dilution refrigerator. For simplicity, we use a square box at the bottom right corner, wherein a pair of qubits is coupled to a coupler, to represent the chip. To control and measure the chip, qubits and couplers are connected to the room-temperature electronics by readout lines (green), microwave-drive lines (blue), fast Z-pulse lines (purple) and slow DC-bias lines (brown). Information on the microwave components is provided in the legend on the right.

As shown in Fig. S6a and b, we use a 3×6 qubit lattice on a flip-chip superconducting quantum processor to implement the theoretical model. This processor has a two-dimensional architecture consisting of a 6×6 qubit array where the nearest-neighbor (NN) qubit pairs are connected by tunable couplers [S19]. Thus, the interaction between each NN qubit pair can be tuned dynamically by applying control signals to the coupler (Fig. S6c), which enables the implementation of two-qubit CZ gates in our experiments. Each qubit is capacitively coupled to a readout resonator for dispersive readout, and each group of nine readout resonators shares a common readout transmission line for simultaneous state measurements. Figure S6c shows the details of the experimental setup, including wiring information, microwave components, and room-temperature control electronics.

B. System calibration

Realizing a well-specified Hamiltonian with digital quantum circuits is a challenging experimental task. It is a complex control problem, whose target is to find optimal parameters which convert time-dependent room-temperature microwave signals to an effective Hamiltonian on the quantum chip at low temperature. In our experiment, we coherently control 45 quantum elements (18 qubits and 27 couplers) for manipulating the topologically ordered Floquet system. Here, we briefly describe our calibration procedures for tuning up these elements.

Before calibrating the universal quantum gate set (single-qubit rotations and two-qubit CZ gate), we use the following procedures to get an overall characterization of the device.

1. Perform spectroscopy measurements for each qubit to obtain the relationship between the qubit frequency ω_q and the amplitude of its fast Z pulse.
2. Tune up each qubit individually at a flux-sensitive point, which we choose ~ 300 MHz below its maximum frequency (sweet point) in our experiments, and perform a series of measurements to obtain the following basic parameters.
 - Single-qubit π and $\pi/2$ pulse parameters.
 - The ratio between the fast Z-pulse amplitude and the slow DC-bias amplitude. With this ratio, we can further get the relationship between qubit frequency ω_q and the amplitude of the DC bias.
 - Qubit readout pulse parameters.
 - Spectrum of T_1 . We note that the T_1 spectrum is repeatedly monitored on different days to detect possible moving two-level-system (TLS) defects [S20].
3. Synchronize the timing of the control pulses from different control lines. We select the center qubit as the root and use the Dijkstra algorithm to traverse all the qubits and couplers from near to far. For the detailed calibration pulse sequences, see Ref. [S21].
4. Calibrate the distortion of the fast Z pulse. Distortion information is obtained by probing the time-domain response of the qubit phase right after a Z pulse [S22]. We note that the distortion of the fast Z pulse for the coupler is derived with the help of the phase response of its adjacent qubits.

With the information above, we can start to tune up the universal quantum gate set on the 3×6 lattice, which includes 18 single-qubit rotations and 27 two-qubit CZ gates. This is challenging due to the existence of pulse distortions, TLS defects, and crosstalk. We allocate a set of idle frequencies $\{\omega_{10}\}$ to qubits, which are optimized to yield high-fidelity single-qubit gates as well as to favor the implementation of two-qubit CZ gates. We consider several important principles, which are listed below.

- Energy relaxation time T_1 and spin-echo pure dephasing time T_2^{SE} in the vicinity of ω_{10} should be long and stable.
- Frequency detuning between two qubits with stray coupling should be much larger than the strength of the stray coupling.
- The fast Z-pulse amplitude for realizing a two-qubit CZ gate should be small to minimize the impact of residue pulse distortion.

In each optimization round, we tune up all the single- and two-qubit gates, and then test their fidelities by performing simultaneous cross-entropy benchmarking (XEB) [S23] using the typical layers in the target circuits. These results are used as the feedback for the next round of optimization. After several rounds, we obtain a set of idle frequencies and gate parameters for our experiments. The idle frequencies $\{\omega_{10}\}$ in this experiment are shown in Fig. S7a. The measured energy relaxation time T_1 and spin-echo dephasing time T_2^{SE} at $\{\omega_{10}\}$ are listed in Fig. S7b and c, respectively. Their cumulative distributions and median values are shown in Fig. S7d, e, and f. Remarkably, the median value of T_1 over 18 qubits is ~ 163 μs . We also achieve median Pauli errors (ϵ_p) of $\sim 0.48 \times 10^{-3}$ for single-qubit gates and $\sim 6.4 \times 10^{-3}$ for two-qubit CZ gates, which is equivalent to the randomized-benchmarking fidelities [S24] of 0.9997 and 0.9949, respectively. Here we use the relation $F = 1 - \epsilon_p / (1 + 1/2^d)$, where d is the number of qubits. Figure S8 shows detailed information on gate errors.

Readout fidelities of qubits are simultaneously measured by preparing 18 qubits in random product states [S25] and averaging them for each qubit. Fig. S9 displays the measured readout fidelities for each qubit in our experiment, which are also used to correct the effects of readout errors.

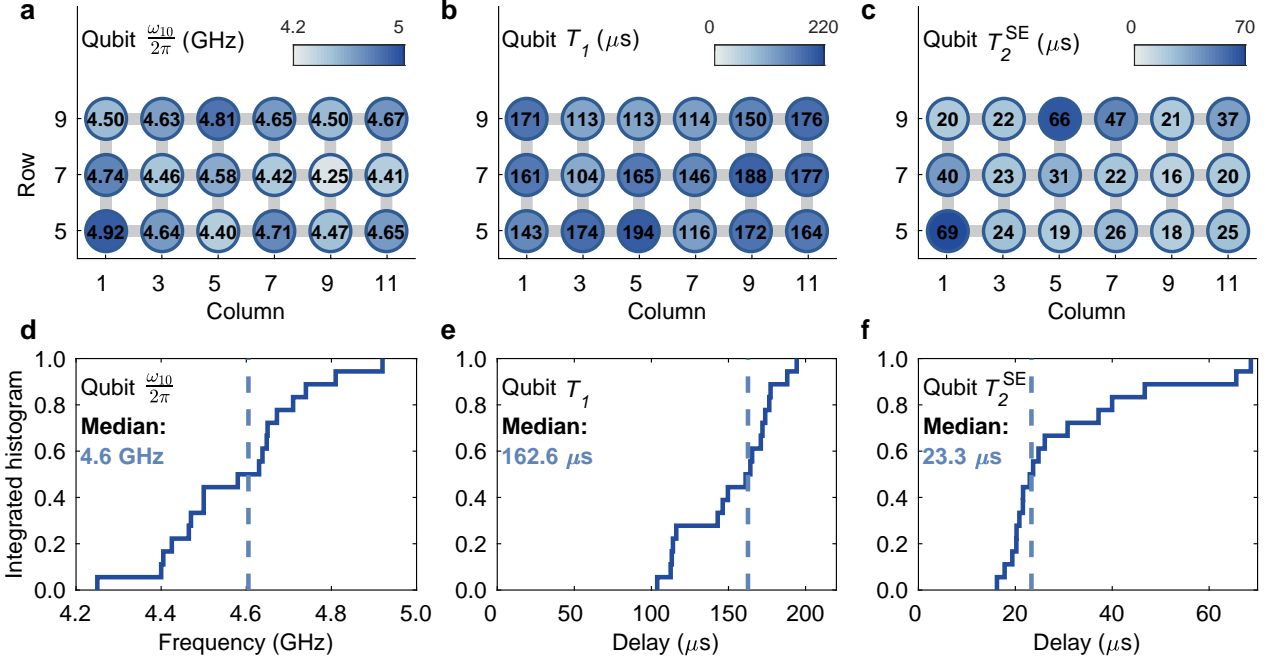


FIG. S7. **Qubit performance at idle frequencies.** **a**, Heat map of idle frequencies $\{\omega_{10}\}$. **b**, Heat map of qubit energy relaxation times $\{T_1\}$ at idle frequencies. **c**, Heat map of qubit spin-echo pure dephasing times $\{T_2^{\text{SE}}\}$ at idle frequencies. **d**, **e**, and **f** are the integrated histograms of $\{\omega_{10}\}$, $\{T_1\}$ and $\{T_2^{\text{SE}}\}$, respectively, which are obtained using the data in **a**, **b**, and **c**.

C. Microwave crosstalk

Single-qubit rotations for each qubit are realized by applying microwave pulses to its microwave drive line. However, microwave pulses applied to Q_i will also induce unwanted state transitions of Q_j . The microwave pulse crosstalk felt by Q_j can be modeled as $\tilde{\Omega}_j = A_{ji}e^{-i\phi_{ji}}\Omega_i$ [S26], where Ω_i is the microwave signal applied to the source qubit Q_i , while $A_{ji}e^{-i\phi_{ji}}$ describes the relative amplitude and the relative phase of the effect on the target qubit Q_j . It can be canceled by actively applying an opposite signal $-\tilde{\Omega}_j$ to the qubit Q_j . We use randomized benchmarking to detect microwave crosstalk, and use the measured matrix $\{A_{ji}e^{-i\phi_{ji}}\}$ to suppress such effects.

D. Flux-bias crosstalk

In our device, applying a bias current to the flux line of qubit Q_i (or coupler C_i) can cause a nonzero flux on other qubits (or couplers). During parallel gate operations, this flux crosstalk can introduce extra phase errors into the circuit. The crosstalk can be modeled as $\tilde{\Delta}_j = \Delta_i B_{ji}$, where Δ_i is the flux to qubit Q_i (or coupler C_i), $\tilde{\Delta}_j$ is the crosstalk flux felt by qubit Q_j , and B_{ji} is the crosstalk ratio. We neglect crosstalk to couplers in our experiments. To compensate for $\tilde{\Delta}_j$, we measure the ratio B_{ji} and apply a flux bias $-\tilde{\Delta}_j$ to Q_j . The measured crosstalk matrix elements $\{B_{ji}\}$ for fast Z bias are shown in Fig. S10.

E. Device-aware circuit transformation

A quantum circuit constructed theoretically usually incorporates little information about the limitations or imperfections of the underlying hardware performance, leaving space for further improvements before it is converted to physical control pulses. Therefore, it is worthwhile to transform the circuits generated in Section I with the awareness of the device information to further

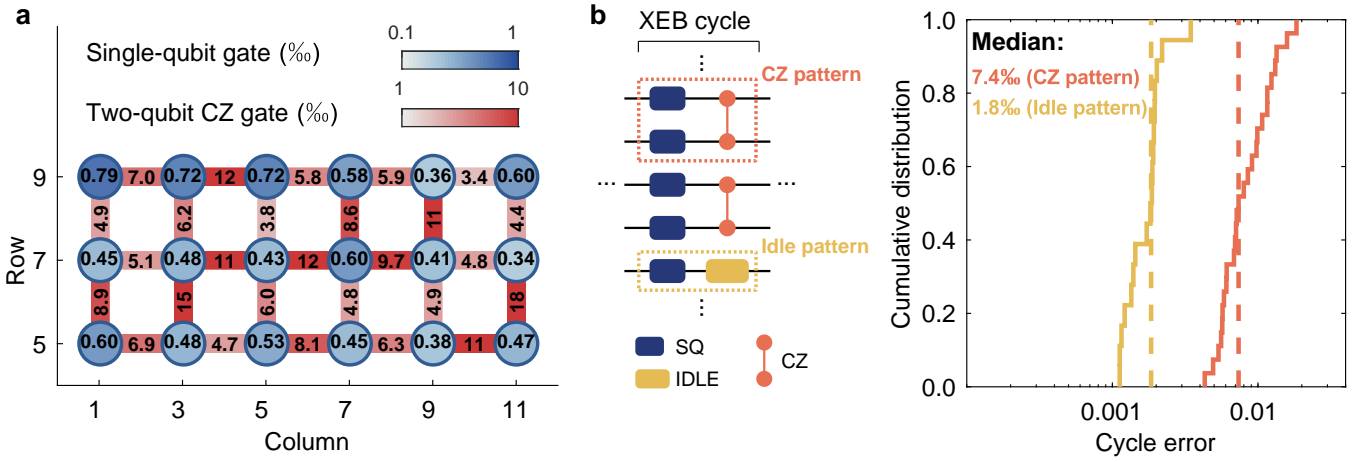


FIG. S8. **Gate errors.** **a**, Heat map of layer-averaged Pauli errors for single-qubit gates (blue) and two-qubit CZ gates (red). These values are measured by performing simultaneous XEB using the typical single-qubit gate layers (SQ layers) and two-qubit CZ gate layers (CZ layers) in the Floquet unitary circuit at $B = 0$ and in the eigenstate preparation circuit. Note that, for the simultaneous XEB of each CZ layer, those qubits that are not involved in CZ gates undergo a single-qubit XEB sequence. **b**, Schematic of the XEB circuit for CZ layers and cumulative distributions of the cycle error. The left panel shows the XEB circuit for the CZ layer. Each cycle is composed of a single-qubit gate layer and a subsequent CZ layer, which includes two types of patterns, a CZ pattern and an idle pattern. The right panel shows the cumulative distributions of cycle errors for the CZ pattern (red) and the idle pattern (yellow). Each data point represents a specific pattern for the target gate, which is averaged over all CZ layers. Using cycle errors, we can estimate CZ gate errors in **a** and idle gate errors in the CZ layers.

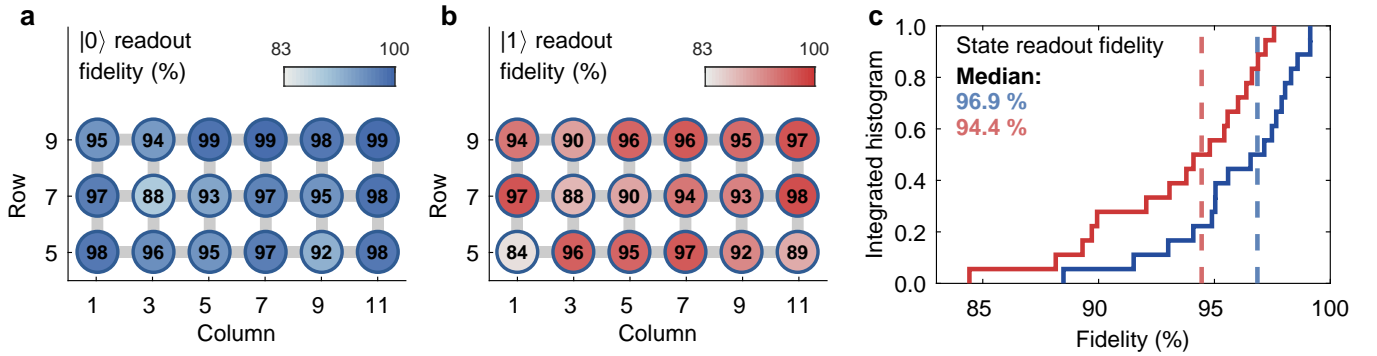


FIG. S9. **Qubit readout fidelity.** **a**, Heat map of the readout fidelity for state $|0\rangle$. **b**, Heat map of the readout fidelity for state $|1\rangle$. **c**, Integrated histogram of 18 readout fidelities based on the data in **a** and **b**. To obtain the readout fidelities, we prepare all the qubits in random computational-basis product states and perform simultaneous measurements. For each qubit, its $|0\rangle$ ($|1\rangle$) readout fidelity is given by calculating the $|0\rangle$ ($|1\rangle$) state probability from the samples that this qubit is prepared in $|0\rangle$ ($|1\rangle$).

improve the circuit fidelity. Figure S11 shows the transformed circuit of the Floquet-evolution unitary for a single period T at $B = 0.1$. We summarize the strategies and tools we use in this process below.

1. Remove redundant Clifford gates using ZX-calculus [S27, S28].
2. Use Qiskit [S29] to convert the circuit into combinations of two-qubit CZ gates and single-qubit rotations around the x, y, z -axis on the Bloch sphere and Cirq [S30] to identify single-qubit layers and separate them from CZ gates. Then we get a circuit that alternates between layers of single-qubit and CZ gates: a single-qubit gate layer (SQ layer), followed by a layer of CZ gates (CZ layer), followed by an SQ layer, etc.
3. Compile consecutive SQ gates into a U3 gate. The U3 gate is constructed by combining a θ -angle rotation around the z -axis followed by an α -angle rotation around an axis in the xy plane with an azimuthal angle ϕ , which can be written in the form

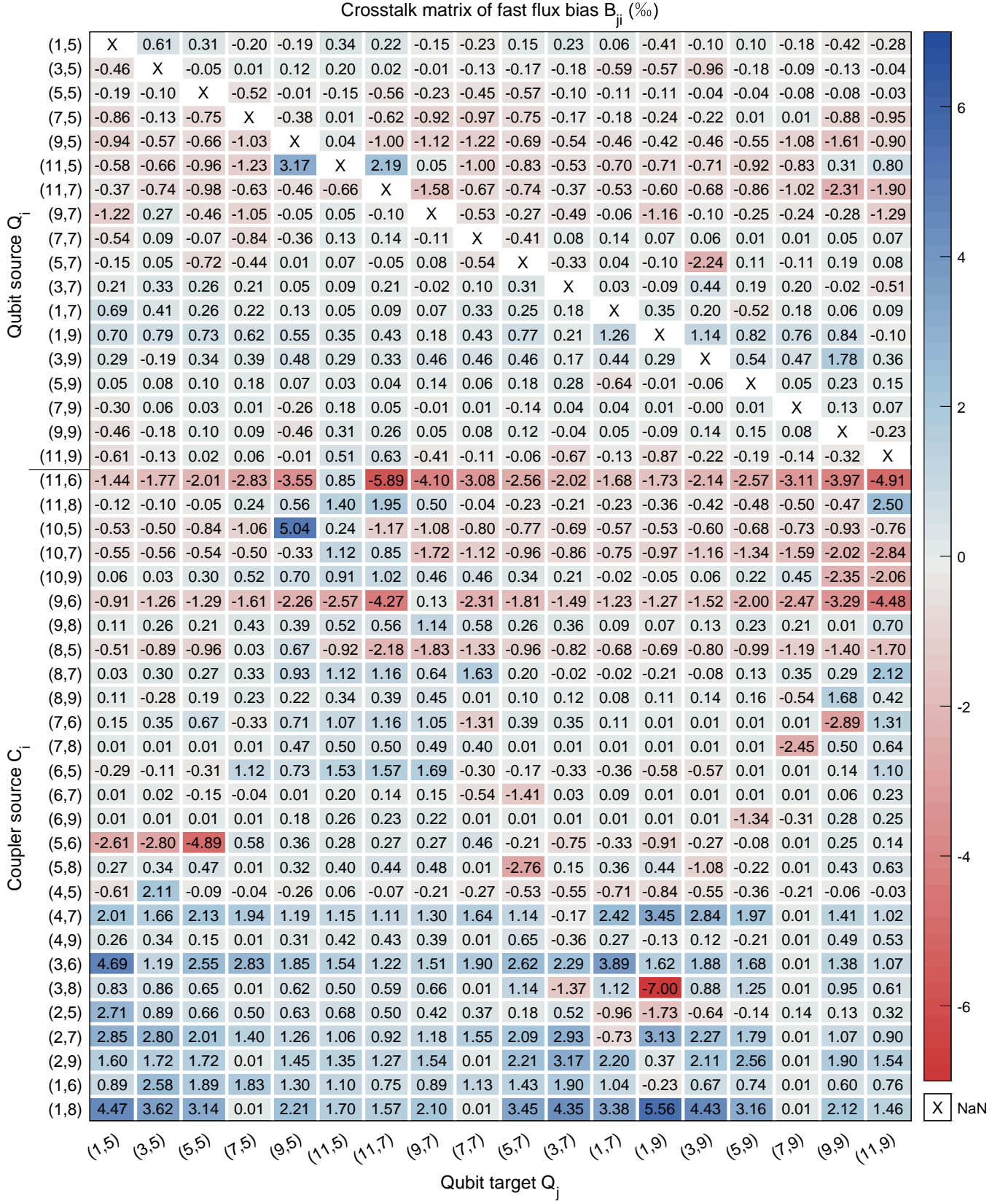


FIG. S10. **Crosstalk matrix of the fast flux bias.** Each qubit (coupler) is labeled by (x, y) , which means it is located in the x -th column and y -th row in our device. Note that we neglect crosstalk to couplers in our experiments.

$$U3(\alpha, \phi, \theta) = R_{xy}(\alpha, \phi)R_z(\theta) = \begin{bmatrix} \cos\left(\frac{\alpha}{2}\right) & -ie^{-i\phi}e^{i\theta}\sin\left(\frac{\alpha}{2}\right) \\ -ie^{i\phi}\sin\left(\frac{\alpha}{2}\right) & e^{i\theta}\cos\left(\frac{\alpha}{2}\right) \end{bmatrix}. \quad (\text{S15})$$

Note that $R_z(\theta)$ is implemented virtually by adding an extra θ to the phase of the subsequent microwave pulse [S31]. $R_{xy}(\alpha, \phi)$ is implemented by applying a microwave pulse, whose phase is ϕ and whose amplitude depends on the rotation angle α .

4. Separate CZ gates in a given layer into several groups. This step is to avoid leakage caused by qubit level crossings while multiple CZ gates operate in parallel. A maximum of two groups are enough for our Floquet-evolution circuit.
5. In the eigenstate circuit, we align the gates to the right of the circuit to delay the first operation on the qubit. Additionally, for quantum state tomography measurements, tomographic rotation is combined with an SQ gate at the end of the circuit, resulting in a U3 gate. To mitigate qubit-dephasing effects, these U3 gates are aligned to the left prior to measurement.
6. To suppress dephasing errors during idling, we incorporate dynamical decoupling (DD) gates. These DD gates are inserted within the circuit, which effectively suppresses the dephasing and thus enhances the overall performance.

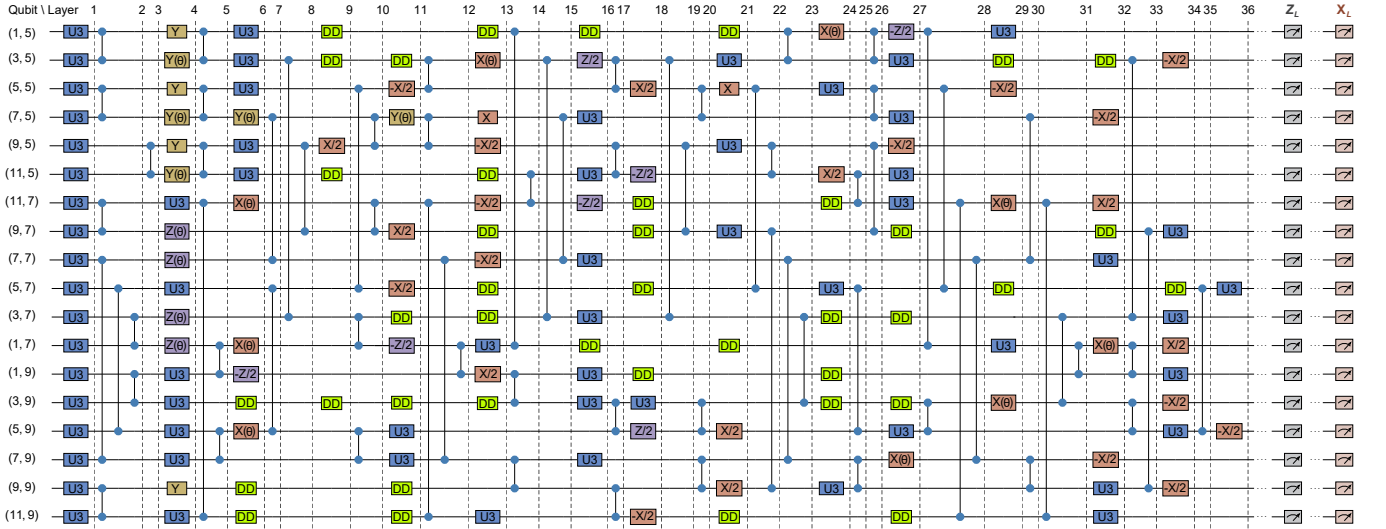


FIG. S11. **Experimental circuit to implement the Floquet unitary U_F at $B = 0.1$.** The first layer of the circuit encompasses the spin-flip driving designed for H_1 , while the subsequent layers of the circuit simulate the evolution of the rotated surface-code Hamiltonian H_2 . U_F is composed of 15 SQ layers and 21 CZ layers. In total, it contains 117 single-qubit gates (excluding 40 dynamical decoupling (DD) gates) and 71 two-qubit CZ gates. We have three types of single-qubit gates: Clifford gates $\{X, Y, Z, \pm X/2, \pm Y/2, \pm Z/2\}$, parameterized rotation gates $\{X(\theta), Y(\theta), Z(\theta)\}$, and $\{U3(\alpha, \theta, \phi)\}$ gates. The DD gates are inserted in pairs. In our experiments, this circuit is repeated up to 20 cycles, for a total of about 2340 single-qubit gates and 1420 CZ gates. This equates to a time-domain sequence of $\sim 28.8 \mu\text{s}$. Note that, at $B = 0$, single-qubit gates in the H_1 circuit are Clifford gates, and thus the whole circuit can be further simplified by merging some of them into the H_2 circuit.

III. NUMERICAL SIMULATIONS

For the experimentally-studied system size, we can numerically simulate the dynamics determined by specifically designed quantum circuits in our experiment. First, classical simulations allow us to evaluate the feasibility of the theoretical proposal by examining whether observables remain discernible after many Floquet cycles under realistic, noisy quantum gates. Second, we can deepen our understanding of our device performance by comparing the experimental results with simulation predictions that incorporate error models.

A. Error model and noisy simulation

We employ the Monte Carlo wavefunction method [S32] to numerically simulate noisy circuits. The idea is to sample error operators according to a noise model and randomly insert them after each ideal gate. In this way, errors occur randomly in the circuit. We evolve the state vector along many quantum trajectories corresponding to many noise realizations. To obtain the value of the desired observable, we average over an ensemble of quantum trajectories, which resembles repeated measurements for evaluating the expectation value of an observable in real experiments. Notably, the Monte Carlo wavefunction method requires fewer computational resources compared to the master-equation approach, because it only stores state vectors of size 2^N during the calculation rather than density matrices of size $2^N \times 2^N$. In this context, we use the state-vector simulator provided by Qiskit for the numerical calculation of system dynamics. Qiskit provides several APIs to construct noise models that approximate the behavior of noisy circuits executed on real NISQ devices.

We model realistic errors with different quantum channels, and represent them with a probabilistic mixture of different operators. The corresponding parameters are estimated using the experimental benchmarks of gate errors and device performance. The following provides an introduction to the error model.

1. **Decoherence errors.** Due to interactions with the environment, energy relaxation and dephasing naturally occur in the dynamics can be described by the quantum channel

$$\mathcal{E}(\rho) = \begin{pmatrix} 1 - \rho_{11}e^{-t/T_1} & \rho_{01}e^{-t/T_2} \\ \rho_{10}e^{-t/T_2} & \rho_{11}e^{-t/T_1} \end{pmatrix} = \sum_{i=0}^3 M_i \rho M_i^\dagger, \quad (\text{S16})$$

where ρ is the density matrix of a single qubit with elements ρ_{ij} ($i, j = 0, 1$). Here, T_1 represents the energy-relaxation time originating from energy exchange with the environment, and T_2 denotes the dephasing time characterizing the damping of off-diagonal terms of the density matrix. They satisfy the relation

$$\frac{1}{T_2} = \frac{1}{2T_1} + \frac{1}{T_\phi}, \quad (\text{S17})$$

where T_ϕ is the pure dephasing time, arising from non-dissipative interactions with the environment. This quantum channel can be written in terms of the Kraus operators

$$\begin{aligned} M_0 &= \sqrt{1 - p_0 - p_1}(|0\rangle\langle 0| + |1\rangle\langle 1|), \\ M_1 &= \sqrt{p_0}|0\rangle\langle 0|, \\ M_2 &= \sqrt{p_0}|0\rangle\langle 1|, \\ M_3 &= \sqrt{p_1}(|0\rangle\langle 0| - |1\rangle\langle 1|), \end{aligned} \quad (\text{S18})$$

which satisfy the normalization condition $\sum_{i=0}^3 M_i^\dagger M_i = I$. The Kraus operator $M_0 \propto I$ indicates that the qubit remains intact with probability $1 - p_0 - p_1$. The pair of Kraus operators M_1 and M_2 describe spontaneous decay of the qubit from its excited state $|1\rangle$ to its ground state $|0\rangle$. This is realized in our simulations by randomly applying a reset operation to the qubit with probability $p_0 = 1 - e^{-t/T_1}$. M_3 contributes an additional dephasing channel to the qubit. Together with the phase damping caused by M_1 and M_2 , $M_{1,2,3}$ describe the total phase damping. M_3 is realized in our simulations by randomly applying σ^z operators with probability $p_1 = \frac{1}{2}e^{-t/T_1}[1 - e^{-t(1/T_2 - 1/T_1)}]$. The two simulation parameters p_0 and p_1 are estimated using the average values of T_1 and T_2^{SE} reported in Section II A, while the value of t is set by the averaged time required to apply an SQ (CZ) layer.

2. **Depolarizing errors.** The depolarizing channel is defined as

$$\mathcal{E}(\rho) = (1 - e_p)\rho + \frac{e_p}{4^d - 1} \sum_{\mu \neq 0} P_\mu \rho P_\mu, \quad (\text{S19})$$

where d is the number of qubits, ρ is a d -qubit density operator, $P_\mu \in \{I, X, Y, Z\}^{\otimes d}$ is the tensor product of Pauli gates, and e_p denotes the Pauli error per cycle. We use the depolarizing channel to account for errors caused by imperfect control of the system, such as gate control errors and crosstalk errors. It is realized in our simulations by applying a randomly chosen non-identity Pauli string with probability $e_p/(4^d - 1)$.

Using the error model above, we perform numerical simulations to verify the observed results in the main text. The decoherence error for each SQ (CZ) layer, quantified by p_0 and p_1 in the model, is estimated with T_1 and T_2 fixed by the average measured T_1 , T_2^{SE} values (see Fig. S7), and with t set by the pulse duration corresponding to an SQ or CZ layer, depending on whether the error channel is being applied after a single- or two-qubit gate layer. The average pulse duration is about 24.0 ns for an SQ layer and 62.6 ns (52.5 ns) for a CZ layer in circuits with (without) eigenstate preparation. Then, the depolarization error rate e_p for each type of gate is estimated by subtracting the decoherence error rate from the median Pauli error rate ϵ_p estimated in the previous section (Section II B). Here, Pauli errors are characterized using XEB experiments (see Fig. S8), whose median value is $\epsilon_p \sim 0.48 \times 10^{-3}$ for a single-qubit gate, 0.64×10^{-2} for qubits involved in a CZ gate, and 1.37×10^{-3} (1.10×10^{-3}) for qubits that are idle during a CZ layer, in experimental circuits with (without) eigenstate preparation. Simulation results using the error sources above are shown in Fig. 2a and Fig. 4b, c, and e of the main text and exhibit good agreement with the experiments.

-
- [S1] X.-G. Wen, Colloquium: Zoo of quantum-topological phases of matter, *Rev. Mod. Phys.* **89**, 041004 (2017).
- [S2] T. B. Wahl, B. Han, and B. Béri, Topologically ordered time crystals, [arXiv:2105.09694](https://arxiv.org/abs/2105.09694) (2021).
- [S3] X.-L. Qi and S.-C. Zhang, Topological insulators and superconductors, *Rev. Mod. Phys.* **83**, 1057 (2011).
- [S4] T. Senthil, Symmetry-Protected Topological Phases of Quantum Matter, *Annu. Rev. Condens. Matter Phys.* **6**, 299 (2015).
- [S5] K. Fujii, Topological stabilizer codes, in [Quantum Computation with Topological Codes: From Qubit to Topological Fault-Tolerance](#) (Springer Singapore, 2015) pp. 56–85.
- [S6] A. G. Fowler, M. Mariantoni, J. M. Martinis, and A. N. Cleland, Surface codes: Towards practical large-scale quantum computation, *Phys. Rev. A* **86**, 032324 (2012).
- [S7] S. Krinner, N. Lacroix, A. Remm, A. Di Paolo, E. Genois, C. Leroux, C. Hellings, S. Lazar, F. Swiadek, J. Herrmann, *et al.*, Realizing repeated quantum error correction in a distance-three surface code, *Nature* **605**, 669 (2022).
- [S8] R. Acharya, I. Aleiner, R. Allen, T. I. Andersen, M. Ansmann, F. Arute, K. Arya, A. Asfaw, J. Atalaya, R. Babbush, *et al.*, Suppressing quantum errors by scaling a surface code logical qubit, *Nature* **614**, 676 (2023).
- [S9] D. Bluvstein, S. J. Evered, A. A. Geim, S. H. Li, H. Zhou, T. Manovitz, S. Ebadi, M. Cain, M. Kalinowski, D. Hangleiter, *et al.*, Logical quantum processor based on reconfigurable atom arrays, *Nature*, **1** (2023).
- [S10] C. Horsman, A. G. Fowler, S. Devitt, and R. V. Meter, Surface code quantum computing by lattice surgery, *New J. Phys.* **14**, 123011 (2012).
- [S11] A. Kitaev and J. Preskill, Topological Entanglement Entropy, *Phys. Rev. Lett.* **96**, 110404 (2006).
- [S12] E. V. H. Doggen, I. V. Gornyi, A. D. Mirlin, and D. G. Polyakov, Slow many-body delocalization beyond one dimension, *Phys. Rev. Lett.* **125**, 155701 (2020).
- [S13] I.-D. Potirniche, S. Banerjee, and E. Altman, Exploration of the stability of many-body localization in $d > 1$, *Phys. Rev. B* **99**, 205149 (2019).
- [S14] W. De Roeck and J. Z. Imbrie, Many-body localization: Stability and instability, *Philos. Trans. R. Soc. Math. Phys. Eng. Sci.* **375**, 20160422 (2017).
- [S15] M. Cerezo, A. Arrasmith, R. Babbush, S. C. Benjamin, S. Endo, K. Fujii, J. R. McClean, K. Mitarai, X. Yuan, L. Cincio, and P. J. Coles, Variational quantum algorithms, *Nat. Rev. Phys.* **3**, 625 (2021).
- [S16] W. Li, Z. Lu, and D.-L. Deng, Quantum Neural Network Classifiers: A Tutorial, *SciPost Phys. Lect. Notes*, **61** (2022).
- [S17] Z. Lu, P.-X. Shen, and D.-L. Deng, Markovian Quantum Neuroevolution for Machine Learning, *Phys. Rev. Appl.* **16**, 044039 (2021).
- [S18] K. J. Satzinger, Y.-J. Liu, A. Smith, C. Knapp, M. Newman, C. Jones, Z. Chen, C. Quintana, X. Mi, A. Dunsworth, *et al.*, Realizing topologically ordered states on a quantum processor, *Science* **374**, 1237 (2021).
- [S19] F. Yan, P. Krantz, Y. Sung, M. Kjaergaard, D. L. Campbell, T. P. Orlando, S. Gustavsson, and W. D. Oliver, Tunable coupling scheme for implementing high-fidelity two-qubit gates, *Phys. Rev. Appl.* **10**, 054062 (2018).
- [S20] P. V. Klimov, J. Kelly, Z. Chen, M. Neeley, A. Megrant, B. Burkett, R. Barends, K. Arya, B. Chiaro, Y. Chen, *et al.*, Fluctuations of energy-relaxation times in superconducting qubits, *Phys. Rev. Lett.* **121**, 090502 (2018).
- [S21] C. Neill, P. Roushan, K. Kechedzhi, S. Boixo, S. V. Isakov, V. Smelyanskiy, A. Megrant, B. Chiaro, A. Dunsworth, K. Arya, R. Barends, *et al.*, A blueprint for demonstrating quantum supremacy with superconducting qubits, *Science* **360**, 195 (2018).
- [S22] R. Barends, J. Kelly, A. Megrant, A. Veitia, D. Sank, E. Jeffrey, T. C. White, J. Mutus, A. G. Fowler, B. Campbell, *et al.*, Superconducting quantum circuits at the surface code threshold for fault tolerance, *Nature* **508**, 500 (2014).
- [S23] S. Boixo, S. V. Isakov, V. N. Smelyanskiy, R. Babbush, N. Ding, Z. Jiang, M. J. Bremner, J. M. Martinis, and H. Neven, Characterizing quantum supremacy in near-term devices, *Nat. Phys.* **14**, 595 (2018).
- [S24] F. Arute, K. Arya, R. Babbush, D. Bacon, J. C. Bardin, R. Barends, R. Biswas, S. Boixo, F. G. S. L. Brandao, D. A. Buell, *et al.*, Quantum supremacy using a programmable superconducting processor, *Nature* **574**, 505 (2019).
- [S25] P. D. Nation, H. Kang, N. Sundaresan, and J. M. Gambetta, Scalable mitigation of measurement errors on quantum computers, *PRX Quantum* **2**, 040326 (2021).
- [S26] Y. Sung, L. Ding, J. Braumüller, A. Vepsäläinen, B. Kannan, M. Kjaergaard, A. Greene, G. O. Samach, C. McNally, D. Kim, *et al.*, Realization of high-fidelity cz and zz-free iswap gates with a tunable coupler, *Phys. Rev. X* **11**, 021058 (2021).
- [S27] A. Kissinger and J. van de Wetering, PyZX: Large scale automated diagrammatic reasoning, *Electronic Proceedings in Theoretical Computer Science* **318**, 229 (2020).
- [S28] A. Kissinger and J. van de Wetering, Reducing the number of non-clifford gates in quantum circuits, *Phys. Rev. A* **102**, 022406 (2020).

- [S29] Qiskit contributors, [Qiskit: An open-source framework for quantum computing](#) (2023).
- [S30] Cirq Developers, [Cirq](#) (2022), See full list of authors on Github: <https://github.com/quantumlib/Cirq/graphs/contributors>.
- [S31] D. C. McKay, C. J. Wood, S. Sheldon, J. M. Chow, and J. M. Gambetta, Efficient z gates for quantum computing, [Phys. Rev. A](#) **96**, 022330 (2017).
- [S32] K. Mølmer, K. Berg-Sørensen, Y. Castin, and J. Dalibard, A monte carlo wave function method in quantum optics, in [Optical Society of America Annual Meeting](#) (Optica Publishing Group, 1992) p. MF1.